NUMERICAL INVESTIGATION OF AIRFLOW AND AEROSOL DEPOSITION CHARACTERISTICS WITHIN HUMAN AIRWAYS

By

Divyajit J. Mahida

Reetesh Ranjan Assistant Professor (Advisor)	Kidambi Sreenivas Professor (Committee Member)

Charles Margraves
UC Foundation Associate Professor
(Committee Member)

NUMERICAL INVESTIGATION OF AIRFLOW AND AEROSOL DEPOSITION CHARACTERISTICS WITHIN HUMAN AIRWAYS

By

Divyajit J. Mahida

A Thesis Submitted to the Faculty of the University of
Tennessee at Chattanooga in Partial
Fulfillment of the Requirements of the Degree
of Master of Engineering

The University of Tennessee at Chattanooga
Chattanooga, Tennessee

May 2021

ABSTRACT

Aerosolized drug delivery in human airways is typically used for the treatment of several pulmonary diseases. In this study, large-eddy simulation (LES) is used for the numerical investigation of the airflow and the aerosol deposition characteristics within the upper human airways. LES is performed using the Eulerian-Lagrangian framework where the airflow is modeled using the Eulerian formulation, and the aerosol evolution is tracked in Lagrangian manner under the dilute suspension conditions using one-way coupled approach. First, the computational framework is assessed in terms of the prediction of the mean flow statistics and the aerosol deposition and comparing with the past experimental and numerical results. Afterward, the effects of inflow Reynolds number (Re) and particle size (d_p) on the deposition fraction (D_F) are examined. The study shows that the effect of Re on D_F is apparent for $d_p > 5$ μm and D_F increases with an increase in d_p.

ACKNOWLEDGEMENTS

First and foremost, I would like to express my sincere gratitude to my advisor Dr. Reetesh Ranjan, for his encouragement, invaluable supervision, patience, and guidance throughout this research. I am also grateful to Dr. Kidambi Sreenivas and Dr. Charles Margraves for agreeing to be on my thesis committee and for their constant support. I am thankful to the members of the Fluids and Combustion Modeling group, namely, Eli Durant, Jash Doshi, Jamie Bowers, for their help and often having a fruitful discussion on problems of common interest.

I would like to express a deep gratitude to Dr. Prakash Damshala, for his exceptional guidance and support during my graduate study. The administrative staff of UTC College of Engineering and Computer Science were always very cooperative. I express my thanks to these staff members. In particular, I appreciate the cooperation and support of Andrea James for her guidance and help at various stages of my graduate study.

I appreciate and acknowledge the support of the Biomedical Research Initiation Collaborative (BRIC) grant from the University of Tennessee at Chattanooga (UTC) for funding this project. Finally, I want to thank SimCenter at UTC for the computational resources and technical support.

TABLE OF CONTENTS

LIST OF FIGURES

LIST OF TABLES

LIST OF ABBREVIATIONS

COPD, Chronic obstructive pulmonary disease

MRI, Magnetic Resonance image

PET, Positron emission tomography

QCT, Quantitative computed tomography

HRCT, High-resolution computed tomography

EL, Eulerian-Lagrangian

EE, Eulerian-Eulerian

DNS, Direct numerical simulation

LES, Large-eddy simulation

RANS, Reynolds averaged Navier-Stokes

SGS, Subgrid-scale

V&V, Verification & validation

WALE, Wall adapting eddy viscosity model

LDA, Laser-Doppler anemometer

PIV, Particle image velocimetry

LBM, Lattice Boltzmann method

LDKM, Locally dynamic kinetic energy model

NM, No-model

FVM, Finite volume method

SIMPLE, Semi-Implicit Method for Pressure-Linked Equations

LRRI, Lovelace Respiratory Research Institute

CT, Computed tomography

SM, Smagorinsky's eddy viscosity model

MPI, Message passing interface

LIST OF SYMBOLS

d_p, particle diameter

d_p, particle diameter

l, integral scale

λ, Taylor-micro scale

η, Kolmogorov microscale

u_i, velocity

p, pressure scaled with density

ν, kinematic viscosity

i, Cartesian coordinate directions

τ_{ij}^{sgs}, subgrid stress

x_{pi}, particle position

v_{pi}, particle velocity

m_p, particle mass

m_f, fluid mass

u_i^+, instantaneous velocity of carrier phase at particle location

τ_p, particle time constant

ν_t, subgrid eddy viscosity

S_{ij}, resolved strain-rate tensor

C_s, Smagorinsky coefficient

c_K Kolmogorov constant

k^{sgs}, SGS turbulent kinetic energy L_{ij}, Leanord Stress

Δt_p, particle time step

Δt_f, flow time step

λ, average expansion ratio of the prism layers Re, Reynolds number

St_{ref}, Stokes number

τ_p, particle response time

$|\langle \widetilde{\boldsymbol{u}} \rangle|$, mean velocity magnitude

D_F, deposition fraction

Q, velocity gradient tensor

$|\langle \widetilde{\boldsymbol{u}} \rangle| / u_B$, normalized mean velocity magnitude

CHAPTER 1

INTRODUCTION

Respiration is a process in living organisms involving the production of energy, typically with the intake of oxygen and the release of carbon dioxide from the oxidation of complex organic substances. It is one of the most basic functions required to sustain life. Breathing and respiratory health are taken for granted, but the lung is an organ that is the most vulnerable to airborne infections leading to different types of pulmonary diseases. Such diseases include asthma, cystic fibrosis, chronic obstructive pulmonary disease (COPD), pulmonary infection, and lung tumors, which occur due to the combined effects of anatomical modification of the airways, bronchial hyper-responsiveness, inflammation, and basilar airflow reduction [3, 4]. According to an estimate, nearly 65 million people suffer from COPD, and 3 million people die from it, making it the third leading cause of death worldwide [5]. In addition, about 334 million people suffer from asthma affecting 14% of the children globally [6]. Effective and efficient treatment procedures are critical to the treatment of such pulmonary ailments.

Several of the pulmonary ailments can be treated by employing aerosolized drug delivery [7], where an improved regional deposition of the inhaled drug is key to maximizing efficiency and minimizing the side-effects of the inhaled drugs. Although recent advancements in radiological imaging techniques such as magnetic resonance image (MRI), positron emission tomography (PET), quantitative computed tomography(QCT), high-resolution computed tomography (HRCT), etc., have enabled an objective assessment of the phenotype of airways and other anatomical features through *in vivo* and *in vitro* measurements, the required information for an effective treatment still tends to be limited. To this end, computational tools can be immensely useful to predict airflow and localized deposition in the respiratory airways as well as in the peripheral regions to optimize the effectiveness of the inhaler therapies [1, 8–26]. However, numerical investigation of such flow systems is extremely challenging due to geometrical complexities, the presence of a wide range of flow features, and aerosol dynamics associated with the inertia of the particles. The present study establishes a computational framework that can capture both airflow and aerosol statistics in such flow systems. Such a predictive framework can provide valuable insight for effective treatment in either prescribing medication or an alternate treatment course.

Aerosol deposition within pulmonary flows corresponds to the broader category of dispersed multiphase flows, which comprise of carrier phase and a disperse phase [27–29]. Such flows can be classified as a dilute suspension, a dense suspension, or a granular flow, depending upon the mass and the volume loading of the dispersed phase. In this study, we consider a dilute suspension approximation with a one-way coupling (only the carrier phase affects aerosol evolution), which is adequate for such flows [1, 21, 23]. Numerical prediction of such flows is still extremely challenging due to the added complexity of the aerosol dynamics to the evolution of the carrier phase flow [1, 21, 23, 27–29]. In particular, the flow field exhibits the presence of features such as laminar to turbulent transition, separation, recirculation, shear-layers, etc., which are difficult to predict [30–32], and in turn significantly affects the aerosol dynamics due to the interaction of the inertial aerosol particles with the flow.

The two well-established approaches for the computational study of such flows include the Eulerian-Lagrangian (EL) and the Eulerian-Eulerian (EE) frameworks [27–29]. While the carrier phase flow is simulated using an Eulerian approach in both these frameworks, the dispersed phase evolution is handled differently in these approaches. In particular, in the EE framework, the dispersed phase is considered a continuum, and transport equations are solved in an Eulerian manner. However, in the EL framework, the dispersed phase is treated as a particle or parcel and is evolved in a Lagrangian manner. In this study, the EL formulation is used to describe the particle evolution where turbulence dispersion, polydispersity, and collision of particles within the airway are easy to model [1, 21, 23].

The carrier phase flow can be simulated using different numerical approaches with varying levels of fidelity and computational costs. These approaches include direct numerical simulation (DNS), large-eddy simulation (LES), and Reynolds averaged Navier-Stokes (RANS). In DNS, all the spatial and temporal scales are resolved, making it suitable for fundamental investigation with reduced geometries in the context of pulmonary flows [16, 24]. In LES, the large-scale structures are explicitly resolved, and the subgrid-scale (SGS) features are modeled, whereas, in RANS, all the turbulent fluctuations are modeled. Past studies have shown the superiority of the LES strategy over RANS in the prediction of the aerosol deposition, particularly for smaller particles [1, 14, 18], and therefore, LES is considered in this study. Note that LES investigations of aerosol deposition in pulmonary systems using the EL framework are still limited in terms of geometric simplification, use of monodisperse particles, one-way coupling to the carrier-phase, simplified Lagrangian transport equations, and neglect of subgrid dispersion [1, 12, 14, 18, 22]. Therefore, further studies are needed to assess and improve the predictive capabilities of such an approach.

To summarize, the present study focuses on investigating aerosol deposition within pulmonary systems using the large eddy simulation (LES) within the Eulerian-Largrangian (EL) framework. Aerosol deposition in the extrathoracic airways occurs due to impaction on the airway walls resulting from the high-velocity magnitude and rapid changes in the flow direction. Typically, the larger particles are more prone to deposition by impaction compared to the smaller particles [1]. Turbulent dispersion plays a significant role [22], particularly for the deposition of the smaller particles whose trajectories are considerably affected by the local velocity fluctuations. The present study first establishes the computational framework by performing verification and validation (V&V) studies by comparing with the past *in vitro* measurements and numerical results for the SimInhale benchmark case [1]. Afterward, the framework is used to examine the effects of Reynolds number and the particle size on the mean flow and particle deposition statistics.

1.1 Key Technical Objectives

This thesis aims to establish the LES-based computational modeling strategy while using the EL framework for the investigation of airflow and aerosol dynamics within the realistic upper human airways. The key technical objectives are as follows:

- **Assessment of modeling strategy:** The goal here is to assess the accuracy of the computational strategy considered in this study. To address this, several simulations have been performed at conditions matching past studies and comparing results for the airflow statistics and the aerosol deposition. The assessment is carried out in terms of examining the role of SGS closure models and the grid resolution. For the SGS closures, the widely popular Smagorinsky model [33], and the locally dynamic kinetic energy model [34] have been considered. In this study we have ignored the role of subgrid turbulence dispersion, which can affect the spatial and temporal evolution of aerosol.

- **Analyze the airflow statistics:** The objective is to examine the airflow behavior observed within human airways, which provides useful *a priori* information in determining medication dose, the injection rate, and injection distribution of the drug. All these parameters are critical for the preferential deposition of the inhaled drug in the diseased regions. Furthermore, detailed information on the airflow, particularly in the peripheral region, can be used to model drug deposition in pulmonary fibrosis and proximal airflow modeling can determine the optimal location for valve placement for lung volume reduction surgery [35]. In particular, the airflow results sensitivity to the employed SGS closures, and the grid and the effect of variation of injection flow rate in terms of inlet Reynolds number (Re) is examined .
- **Characterize the effects of injection flow rate and particle size:** To treat pulmonary ailments, specific regions and sometimes peripheral areas are of interest where the drug needs to be delivered. Furthermore, it is also required that the inhaled drug does not get deposited in healthier regions to minimize the side effects. However, the inhaled drug may not reach specific regions depending upon the effects of airflow

on the aerosol evolution. The variation of injection flow rate in terms of inlet Reynolds number (Re) and the particle size in terms of diameter (d_{p}) can alter the particle characteristic time scales, which in turn can affect the aerosol dynamics by altering the local Stokes number, which is a critical parameter that governs particle dynamics [27–29]. Therefore, further investigation is carried out to characterize the role of Re and d_{p} on the global and the local aerosol deposition fraction in different segments of the human airways.

1.2 Thesis Layout

The thesis is organized as follows. The current state-of-the-art pertaining to the investigation of airflow and aerosol characteristics within human airways is discussed in chapter 2. The governing equations, subgrid models, and numerical methodology considered in this study are described in chapter 3. The details of the computational setup are described in chapter 4. Chapter 5 discusses the results from the V&V studies. The effects of inlet Re and d_{p} on the airflow and aerosol statistics are described in chapter 6. Finally, the key accomplishments of this study and the future directions are summarized in chapter 7.

CHAPTER 2

AIRFLOW AND AEROSOL DEPOSITION IN AIRWAYS

Aerosol deposition within the human airways corresponds to the category of the dispersed multiphase flows, also referred to as particle-laden flows. In such flows, the two phases are referred to as the carrier phase, and the dispersed (particle) phase and the interphase dynamics are of secondary importance. To examine the characteristics of airflow and aerosol dynamics in such flows, several studies, including analytical, experimental, and computational have been performed in the past. A detailed survey of past studies and their key findings can be found in the review articles [1, 21, 23]. Here, we first summarize the numerical approaches that the past studies have considered for the investigation of this particular particle-laden flow configuration. Afterward, we provide a brief review of the key findings of the past studies.

2.1 Modeling of Airflow

The upper part of the human airway, also referred to as the extra-thoracic airway, includes nasal passages, mouth-throat region, larynx, pharynx, trachea, and carina. The inhaled and exhaled air passes through the nose or mouth as the main inlet. A detailed understanding of the airflow characteristics is required before modeling pathogenesis of respiratory diseases [36, 37]. In the upper airways, the flow is mostly turbulent or transitional in nature, even at a very low inhalation rate [38]. In fluid dynamics, turbulent flow is characterized by chaotic changes in the flow field. It contrasts with the laminar flow, which occurs when the fluid flows in parallel layers, with no disruption between those layers. In particular, a turbulent flow is characterized by different types of length scales, such as the integral scale (l), the Taylor micro-scale (λ), and the Kolmogorov microscale (η). It is usually impossible to resolve all the small scales in the flow, particularly, in the complex airway geometry. Therefore, we have considered adopting an accurate and robust turbulence modeling strategy.

To computationally model the airflow dynamics in the upper airways or parts of it, three methods are usually considered, which include the RANS, LES, and DNS techniques. These approaches are listed in the increasing order of fidelity of description and the computational cost. Although the most accurate method to represent the underlying structure of turbulence and particle transport in turbulent flow is DNS, it is usually relegated to investigating the fundamental physics of turbulence and associated transport processes in canonical configurations and at low to moderately high Re. In RANS, all turbulent fluctuation is modeled, mainly based on the empirical data from canonical flows or other equilibrium flows, thus making it a computationally tractable approach for design studies. The large-eddy simulation (LES) approach separates large-scale, and small-scale components of turbulent flow field through a filtering process, and the large energy-containing scales of motion are calculated directly while the effect of the small subgrid scales of motion is modeled. Thus the LES prediction is less sensitive to modeling error compared to the RANS calculation, and since the subgrid-scale is universal than the large scale, it is possible to represent the effect of the subgrid-scale using a relatively simple model. Here, we focus on using a modeling approach instead of relying on DNS to investigate the airflow dynamics. However, in a RANS, all of the turbulent fluctuations are modeled thus the evolution of particles in airways and their subsequent deposition can be significantly affected. A significant advantage of LES over RANS is that it permits a much more accurate accounting of particle-turbulence interaction [39]. Therefore, LES tends to be a relatively accurate approach when particles unsteady dynamics and the effects of turbulent fluctuations on the deposition are significant.

As mentioned before, in LES, the large energy-containing scales are computed directly, while the subgrid-scale (SGS) models represent the dynamical effects of the smaller scales resulting from the filtering operation. Past LES based studies of airflow in human airways [1, 13, 14, 18, 22, 25] have primarily considered the well-established SGS models, which include the Smagorinsky eddy viscosity model [33], the dynamic eddy viscosity model [40], and wall adapting eddy viscosity based model (WALES) [41]. Note that LES of high Re, complex wall-bounded flows, such as those observed in human upper airways face certain unresolved challenges. The challenges are a realistic representation of subgrid stress tensor [42], to accurately resolve the dynamically dominant near-wall structures [43] and modeling laminar-to-turbulent transition and the transition between near-wall and far-field free shear flows without requiring *ad hoc* fixes.

2.2 Modeling of Aerosol Dynamics

The key mechanisms for aerosol deposition in the human airways include impaction and dispersion. The impaction occurs due to higher velocity magnitude and rapid changes in the flow direction. The particles tend to deviate from the streamline of the flow field and collide with the walls due to their inertia leading to the subsequent deposition. As the size of the particle increases, the probability of deposition due to impaction also increases. However, the turbulent dispersion plays a crucial role in the smaller particle's deposition as the underlying flow field fluctuations considerably influence their trajectories.

The transport of particles in the upper airway can be modeled with the Eulerian or the Lagrangian approach. The Eulerian or two-fluid approach models both the dispersed (particles) and the carrier phases as continuous phases, solving the coupled conservative equations for both the phases. On the other hand, in the Lagrangian approach, the dispersed phase is treated as an individual point particle in the continuous carrier phase. The particles are tracked in the fluid flow by solving the equation of motion for each particle with relevant forces acting on them [27, 29]. There are three different coupling possibilities between the carrier and the dispersed phases: 1) one-way coupling where the fluid flow affects the particle, 2) two-way coupling where the fluid flow affects the particle, and the particles affect the fluid flow, 3) four-way coupling where the particles affect the flow and *vice-versa* and the particles also affect the neighboring particles through collision. The Lagrangian approach is more naturally suited for depicting the turbulent dispersion and the collision of particles with the walls in the upper airway model. Due to this, most of the past studies have used the Lagrangian approach for modeling the aerosol deposition in the upper airways [11, 15, 18, 26, 39]. In these studies, the particles are assumed to be spherical, non-interacting, and non-rotating. The particles are modeled with one-way coupling, which means that the effect of the particle on the flow is neglected. However, in reality, the aerosol particles are usually not spherical and may collide with each other making it a four-way coupled particle-laden flow. In the present study, we have followed the past studies and considered a one-way coupled particle-laden turbulent flow scenario.

2.3 Key Findings of Past Studies

In this section, we summarize the key observations of the past experimental and computational studies.

2.3.1 Experimental Studies

A flexible model of the upper airway is challenging to investigate. Therefore, most of the past experimental studies have been carried out using a rigid airway. Such studies have mainly focused on measuring the quantities such as the mean velocity and Reynolds stress of the carrier phase, particle velocity, and particle concentration in different regions of the flow. One of the earliest attempts was through *in vivo* clinical observation, where the distribution of inhaled powder in nasal cavities was examined. Very little could be learned through these experiments due to the complexity of the human airway [44, 45]. Therefore, researchers started using the *in vitro* models of the nasal cast, which was usually obtained from cadavers. In these life-size models, smoke was released through the nasal cavities to examine the flow field such as the presence of recirculating flow regimes [45, 46].

The adaptation of laser-based flow measurement techniques has revolutionized the experimental studies of turbulent dispersed flow. A laser-Doppler anemometer (LDA) measures the velocity of the dispersed particles. LDA can be easily adapted for larger particles ($d_p > 5\mu m$) as larger particles scatter more light, which produces stronger signals [29]. To study the carrier phase, one adds a fine tracer particle. The LDA signal processing discriminates between the Doppler burst produce by the dispersed particle and the tracer particle. Usually, the Doppler signal amplitude is much smaller for the tracer element than the dispersed particle. For measuring the velocity of both phases, the photo-detector output is fed to two separate processors. One processor is set for low gain, detecting the particle, while the other detects the tracer element. Girardin et al. [47] used LDA to determine velocity field in the human nasal cavity model made out of cadaver. Measurements were taken at one flow condition and five coronal sections. They observed that the flow was more significant in the lower half of the fossa and closer to septum regions. Furthermore, it was observed that the velocity fields appear to give more information on the intra-nasal aerodynamics than the Reynolds number and the calculated flow field [47].

Recently, particle image velocimetry (PIV) has been preferred over laser-Doppler anemometer (LDA) as it measures the velocity of both the phases simultaneously over an imaged area. For dilute flow, a larger particle produces a bright image using conventional cameras and laser, easy to interpret. Similarly, like LDA, PIV also faces difficulty while measuring the velocity of the carrier phase. Most problems are encountered while measuring the carrier-phase velocity near the particle surface. Turbulent kinetic energy dissipation rate is vital for understanding turbulence modulation by particles, which is difficult to measure because it requires spatial derivatives of all velocity components. Paris [36] tried direct calculation of dissipation from particle image velocimetry (PIV) but found that the measured dissipation rate was sensitive to PIV spatial resolution. Brucker and Park [48] used the PIV method to investigate the velocity field in the human nasal cavity. To overcome the difficulties of digital PIV measurements in the air medium, they used liquid instead of air

(Tetrahydronaphtalene was used as the carrier medium). As the model was constructed using low-resolution anatomical data, they observed high velocity in the olfactory region, which is uncommon.

Stereo PIV, usually provides 2D data. The newly developed tomographic PIV technique can obtain 3D measurements. Kim and Chung [49] investigated the airflow in normal and abnormal nasal cavities by tomographic PIV. Average and root mean square distribution of velocities in both sagittal, as well as coronal planes, were obtained for inspiratory and expiratory nasal airflow. Later Kim and Chung [50] extended their previous study [49] where tomographic measurements were taken for the nasal cavity to a full respiratory model that extends from the nasal cavity on the superior to the trachea in the inferior end. They observed that the mainstream went through the backside of the larynx and trachea in inspiration and the frontal side in expiration during respiration cycles. Averaged and root-mean-square velocity flow distributions in both coronal and sagittal planes were obtained during seven temporal points along the respiratory cycle.

There have been several advances in experimental measurement techniques for the simultaneous measurement of the velocity of both the carrier and the dispersed phases. However, measurement of the carrier-phase velocity near the particle remains a significant issue that has to be addressed separately for each new experiment [29]. Radiological imaging techniques can also be applied in the *in vivo* experiments to obtain deposition measurements for validation. The *in vivo* measurements are of great importance as they can describe the real state, but studies remain limited by spatial and temporal resolutions of current imagining techniques and patient exposure to radiation [1].

2.3.2 Computational Studies

As mentioned in Sec. 2.1, Direct Numerical Simulation (DNS) is computationally prohibitive as it requires a very fine mesh to resolve all the scales of motion in the flow. Therefore, only a few DNS studies have been done on the human airway, where the geometry is simplified for computational tractability. For example, Lin et al. [16] compared the flow in the upper and intra-thoracic airways. The geometry included the mouth and the throat regions with the intra-thoracic airway. It was observed that turbulence induced by the laryngeal jet significantly affects the airway flow patterns and trachea wall shear stress. Thus airflow modeling, particularly subject-specific evaluations, should consider upper as well as intra-thoracic airway geometry. Ball et al. [51] used the lattice Boltzmann method (LBM) to conduct a DNS of the airflow inside an idealized human upper airway. LBM simulation results were compared to those from experimental results [52]. The LBM results yield better results for the mean flow statistics compared to the RANS methods. Nicolaou and Zaki [24] performed DNS in realistic mouth-throat geometry, where it was shown that the geometric variation has an enormous impact on both the mean velocity profiles and the turbulence intensities.

Two RANS models have been used for simulating the flow in the airway geometry. These include the well-established k-ϵ and the k-ω model. The k-ϵ model-based RANS has been performed for the upper airway by Finlay et al. [53], where they found that most of the model is designed for high *Re* flow in simple geometry, which makes it unsuitable for low *Re* turbulence in complex geometry such as the upper airway. Finlay [53] observed RANS yield poor results with inflows having recirculating regions, free-shear layers, and mean streamline curvature, all of which are present in the airway flow. Stapleton et al. [9] studied the suitability of k-ϵ turbulence model for aerosol deposition in the mouth and throat regions and compared it with the experimental results. Two simulations were performed corresponding to laminar flow and turbulent flow conditions. Overall, good agreement was obtained for the laminar case but not for the turbulent case. The measured and predicted pressure drop agreed well for the laminar condition but differed slightly for turbulent flow conditions. The laminar case showed good agreement with the *in vitro* measurements, but the turbulent flow case over-predicted the particle deposition. The principal difficulty in predicting particle-laden turbulent flow is that RANS models using gradient hypotheses do not accurately account for the complex interaction between particle and turbulence [39]. Another major shortcoming of the RANS model is the prediction of the properties of the Eulerian turbulence field.

Most of the upper airway studies have used micron-sized particles and have taken into account only the gravitational and drag forces and neglected all the other forces [11, 15, 26]. Some studies have only considered dynamic drag force and neglected even the gravitational forces [17, 54]. For example, Ma and Lutchen [55] simulated aerosol deposition in human airway with and without gravitational force and concluded that when the gravity was ignored, there was a 10% reduction in the total deposition. While drag force's impact is significant for deposition in the upper airway, we cannot ignore the effects of gravitational force. For larger particles, gravity's effect is more significant, and its effect decreases with a higher flow rate. Due to the large particle-fluid density ratio for aerosol particles in the air, the Saffman lift, pressure gradient, added mass, and Basset forces are typically considered insignificant in the upper airways [53]. Jayaraju et al. [18] simulated fluid flow in normal breathing conditions in the human mouth-throat model using LES (Large Eddy Simulation) and RANS (Reynolds-Averaged Numerical Simulation) approaches. Velocity and kinetic energy showed good agreement with LES while less so with RANS as compared with the experimental data. Particle deposition has been examined with particle diameter from 2 to 10 μm. In comparison with the experimental data, LES showed better results than RANS in predicting deposition for particle size below 5 μm. For large size particles, RANS and LES model showed similar predictions as compared with the experimental results. Since the upper limit for the particle size for the inhalation drug is 5 μm, LES is considered a better option than the RANS model [18].

CHAPTER 3

FORMULATION AND NUMERICAL METHODOLOGY

In this chapter, first, the governing equations for LES within the EL framework are described. Afterward, SGS closure models considered in this study are discussed. Finally, a description of the numerical methodology employed in this study to solve the governing equations is presented.

3.1 Governing Equations

A one-way coupled particle-laden turbulent flow is considered in this study, which is a valid approximation under dilute conditions. In such a flow, the carrier phase affects the dispersed phase's dynamics, whereas the dispersed phase does not affect the carrier phase. The interaction between the dispersed phase in terms of the particle to particle collisions is also neglected in this study. Here, the carrier phase is considered an incompressible fluid, and the dispersed phase comprises spherical particles with uniform diameter and density.

3.1.1 Equations for Carrier Phase

In Large-Eddy Simulation (LES), the spatial filtering of a field variable $\phi(\boldsymbol{x}, t)$ leads to the resolved field $\overline{\phi}(\boldsymbol{x}, t)$ and the unresolved SGS field $\phi'(\boldsymbol{x}, t)$, which are related through: $\phi'(\boldsymbol{x}, t) = \phi(\boldsymbol{x}, t) - \overline{\phi}(\boldsymbol{x}, t)$. In the present study, a box filter is used with filter width $\overline{\Delta}$, which corresponds to a local volume-averaging operation in the physical space, and has a global support in the spectral space. Additionally, an implicitly filtered LES formulation is considered here, which uses the computational grid as the filter. Applying the spatial filtering operation to the incompressible Navier-Stokes equation leads to the following filtered LES equations for the carrier phase

$$\frac{\partial \overline{u}_i}{\partial x_i} = 0, \tag{3.1.1a}$$

$$\frac{\partial \overline{u}_i}{\partial t} + \frac{\partial \overline{u}_i \overline{u}_j}{\partial x_j} = -\frac{\partial \overline{p}}{\partial x_i} + \nu \frac{\partial^2 \overline{u}_i}{\partial x_j \partial x_j} - \frac{\partial \tau_{ij}^{\text{sgs}}}{\partial x_i}. \tag{3.1.1b}$$

Here, u_i is the velocity component, p is the pressure scaled with density, ν is the kinematic viscosity, and $i = 1,\ 2,\ 3$ denotes Cartesian coordinate directions. The term $\tau_{ij}^{\text{sgs}} = \overline{u_i u_j} - \overline{u}_i \overline{u}_j$ denote the SGS stress, which require further modeling to close the LES equations.

3.1.2 Equations for Dispersed Phase

The dispersed phase is governed by the following equations for the position ($x_{\text{p}i}$) and velocity ($v_{\text{p}i}$) of particles

$$\frac{dx_{\text{p}i}}{dt} = v_{\text{p}i}, \tag{3.1.2a}$$

$$m_{\text{p}} \frac{dv_{\text{p}i}}{dt} = m_{\text{p}} \frac{\phi(Re_{\text{p}})}{\tau_{\text{p}}} \left(u_i^+ - v_{\text{p}i}\right) - g(m_p - m_f)\delta_{i2}, \tag{3.1.2b}$$

where, m_{p} is the particle mass, m_{f} is the fluid mass, u_i^+ is the instantaneous velocity of the carrier phase at the location of the particle, $\tau_{\text{p}} = \dfrac{d_{\text{p}}^2}{18\nu} \dfrac{\rho_{\text{p}}}{\rho}$ is the particle time constant and $\phi(Re_{\text{p}})$ is an empirical correlation used to modify the Stokes drag for large Re_{p} with

Re_p being the particle Reynolds number, and g is the magnitude of the acceleration due to gravity. Here, a large particle to fluid density ratio (ρ_p/ρ) is considered. Furthermore, other terms such as unsteady drag, added mass, Basset history forces are neglected as the effects of such forces on the evolution of particles are negligible for large ρ_p/ρ.

The particle Reynolds number Re_p is defined as

$$Re_p = \frac{\rho_p d_p \left| u_i^+ - v_{\mathrm{p}i} \right|}{\rho \nu}, \tag{3.1.3}$$

and the empirical correlation $\phi(Re_\mathrm{p})$ is given by [56]

$$\phi(Re_\mathrm{p}) = \begin{cases} 1 + \frac{1}{6} Re_p^{\frac{2}{3}}, & Re_\mathrm{p} \leq 1000 \\ 0.424 \frac{Re_\mathrm{p}}{24}, & Re_\mathrm{p} \geq 1000 \end{cases}. \tag{3.1.4}$$

3.2 Subgrid Modeling

In this study, two different closure models are used to model the subgrid scale (SGS) stress tensor. These models correspond to the algebraic (SM) and the one-equation-based closures (LDKM),

3.2.1 Modeling of SGS Stress

A well-established and popular approach to close the SGS stress tensor τ_{ij}^{sgs} is to use the gradient diffusion hypothesis through:

$$\tau_{ij}^{\mathrm{sgs}} - \frac{\tau_{kk}^{\mathrm{sgs}}}{3} \delta_{ij} = -2 \nu_t \overline{S}_{ij}. \tag{3.2.1}$$

Here, ν_t is the subgrid eddy viscosity, and

$$\overline{S}_{ij} = \frac{1}{2}\left(\frac{\partial \overline{u}_i}{\partial x_j} + \frac{\partial \overline{u}_j}{\partial x_i}\right) \tag{3.2.2}$$

is the resolved strain-rate tensor. A classical method to obtain ν_t is to use Smagorinsky algebraic model [33], which relates ν_t to the magnitude of the resolved strain-rate tensor and the employed grid resolution through:

$$\nu_t = C_s \overline{\Delta}^2 |S|, \text{ where } |S| = \sqrt{2\overline{S}_{ij}\overline{S}_{ij}}, \tag{3.2.3}$$

where C_s is the Smagorinsky coefficient. To obtain C_s, the rate of energy transfer from large scale to small scale is set equal to the rate of viscous dissipation, which leads to

$$C_s = \left(3 c_K \pi^{\frac{4}{3}}/2\right)^{\frac{-3}{4}} \approx 0.16, \tag{3.2.4}$$

where the empirical value of Kolmogorov constant $c_K \approx 1.6$ is used [57]. However, this is only valid for isotropic turbulent flows. For other types of non-homogeneous turbulent flows such as wall-bounded, shear or transitional flows, the value of C_s produces higher dissipation. In such cases, C_s can be determined in a dynamic manner as proposed by Germano et al. [58]. Alternatively, a closure of ν_t can be obtained by relating it to the SGS turbulent kinetic energy k^{sgs} through [59]

$$\nu_t = C_\nu \overline{\Delta} \sqrt{k^{\mathrm{sgs}}}, \tag{3.2.5}$$

where $k^{\mathrm{sgs}} = \frac{1}{2}\left(\overline{u_k u_k} - \overline{u}_k \overline{u}_k\right) = \frac{\tau_{kk}^{\mathrm{sgs}}}{2}$. An additional modeled transport equation is solved to determine k^{sgs} [34, 59, 60], and the coefficient C_ν is determined locally (both in space and time) in a dynamic manner using the locally dynamic kinetic energy model (LDKM) [34, 60].

In the present study, Smagorinsky and LDKM approaches are considered for the closure of τ_{ij}^{sgs}. While a detailed description of these approaches is provided in the cited references, next, we provide further details of the one-equation-based LDKM for the closure of the SGS stress.

In the LDKM [34, 60], a modeled transport equation for k^{sgs} [59] is solved to determine ν_t through Eq. (3.2.5). This equation is given by

$$\frac{\partial k^{\mathrm{sgs}}}{\partial t} + \frac{\partial}{\partial x_j}\left(u_j k^{\mathrm{sgs}}\right) = -\tau_{ij}^{\mathrm{sgs}} \overline{S}_{ij} + \frac{\partial}{\partial x_j}\left[\left(\nu + \nu_t\right) \frac{\partial k^{\mathrm{sgs}}}{\partial x_j}\right] - C_\epsilon \frac{\left(k^{\mathrm{sgs}}\right)^{3/2}}{\overline{\Delta}}. \tag{3.2.6}$$

In the right-hand-side of the above equation, the three terms denote production, molecular and turbulent diffusion, and dissipation of k^{sgs}, respectively. Furthermore, C_ϵ is another model coefficient, which is also determined dynamically in a similar manner to the other model coefficient C_ν [34]. To determine the two model coefficients, test filter fields are used, where the test filter ($\hat{\Delta}$) is consistent with the grid filter ($\overline{\Delta}$). It is prescribed as $\hat{\Delta} = 2\overline{\Delta}$ [58]. Here, we briefly describe this procedure, and for further details, the reader is referred to the cited references.

The Leonard stress after application of the test-filter is given by

$$L_{ij} = \widehat{\overline{u}_i \overline{u}_j} - \widehat{\overline{u}}_i \widehat{\overline{u}}_j, \tag{3.2.7}$$

where $\widehat{(\cdot)}$ denotes the test-filtering operation. In Eq. (3.2.7), all the terms are known. Afterwards, based on the experimental observations [61], a scale similarity assumption is employed to relate the Leonard stress L_{ij} with the SGS stress τ_{ij}^{sgs} to determined the model coefficients. Due to the application of test-filtering, the test-filtered kinetic energy can be defined as

$$k^{\text{test}} = \frac{1}{2}\left(\widehat{\overline{u}_k\overline{u}_k} - \widehat{\overline{u}}_k\widehat{\overline{u}}_k\right) = \frac{1}{2}L_{kk}, \tag{3.2.8}$$

which is similar to k^{sgs}, but is fully resolved at the test filter level. Due to the assumed similarity of L_{ij} and τ_{ij}^{sgs}, the Leonard stress tensor can be expressed in a manner similar to Eq. (3.2.1) yielding

$$L_{ij} = -2C_\nu\widehat{\Delta}\sqrt{k^{\text{test}}}\widehat{\overline{S}}_{ij} + \frac{1}{3}\delta_{ij}L_{kk}. \tag{3.2.9}$$

The above equation explicitly provides a way to determine the model coefficient C_ν, as the other terms are known. However, it is an over-determined system of equations, and therefore, C_ν is obtained approximately using the least-square method leading to

$$C_\nu = \frac{1}{2}\frac{L_{ij}M_{ij}}{M_{lm}M_{lm}}, \tag{3.2.10}$$

where $M_{ij} = -\widehat{\Delta}\sqrt{k^{\text{test}}}\widehat{\overline{S}}_{ij}$. To determine the other model coefficient C_ϵ, which is required for closure of the subgrid scale (SGS) dissipation of the turbulent kinetic energy, i.e., ϵ^{sgs}, we employ similarity between the turbulent kinetic energy ϵ^{sgs} and the dissipation of k^{test}, which is given by

$$E = (\nu + \nu_t)\left(\widehat{\frac{\partial \overline{u}_i}{\partial x_j}\frac{\partial \overline{u}_i}{\partial x_j}} - \frac{\partial \widehat{\overline{u}}_i}{\partial x_j}\frac{\partial \widehat{\overline{u}}_i}{\partial x_j}\right), \tag{3.2.11}$$

and can be modeled in the following manner,

$$E = C_\epsilon \frac{\left(k^{\mathrm{test}}\right)^{3/2}}{\widehat{\Delta}}, \tag{3.2.12}$$

in the above equation, the only unknown is C_ϵ, which can be now determined as all other terms are known.

Note that the LDKM formulation is well-posed and does not require algorithmic adjustments such as spatial averaging along homogeneous directions [60]. In terms of the computational cost, the LDKM formulation has an extra cost compared to the Smagorinsky model, which is associated with the solution of the transport equation for k^{sgs}. However, it has the advantage over the algebraic approach as the equilibrium assumption is not required. Finally, k^{sgs} provides a more accurate estimate for the SGS velocity scale, which can be used for problems related to turbulence interaction with other transport processes such as heat transfer, mass transfer, combustion, etc., and modeling of the subgrid dispersion.

3.2.2 Modeling of Subgrid Dispersion

It is apparent from Eq. (3.1.2)(b) that the coupling between the carrier and the dispersed phase is through u_i^+, which needs to be computed at the location of the particle at each time step. While performing Direct Numerical Simulation (DNS), it is obtained by interpolating instantaneous velocity u_i from the computational grid to the location of the particle. However, while performing LES, u_i is not available as LES only solves for the filtered velocity field $\overline{u}_i$, thus requiring an approximation of u_i^+. The models used for solving subgrid dispersion can be grouped into two main categories, structural and stochastic [62]. The structural models are aimed at reconstructing the entire subfilter velocity field while the stochastic model is aimed at retrieving only some statistical feature of the subfilter velocity field [63].

In the present study, we have considered the no-model (NM) strategy, which completely neglects the effects of subgrid dispersion. Therefore, the approximation of u_i^+ is given by

$$u_i^+ = \overline{u}_i, \tag{3.2.13}$$

such an approach in an LES can lead to inaccuracies in the prediction of particle dynamics, particularly when the SGS kinetic energy is significant or the particle time constant is small [64]. Both these conditions are prevalent in LES of practically relevant flows where usually coarse grids are used for computational efficiency. However, as a first step to establish the computational strategy, we have considered this simplified approach. Future studies will examine the role of subgrid dispersion models on aerosol deposition characteristics.

3.3 Numerical Methodology

We use the Eulerian-Lagrangian framework of the OpenFOAM software framework [65] to carry out simulations in this study. The solver is extended in this work for LES of particle-laden flows using the Eulerian-Lagrangian (EL) formulation by extending the baseline solver for the unsteady incompressible turbulent flows. The details of the Eulerian and Lagrangian solver are provided below.

3.3.1 Eulerian Solver Description

The governing equation for the carrier phase given by Eq. (3.1.1) is spatially discretized using the finite volume method (FVM). One of the essential features of the FVM is it can be easily formulated for unstructured meshes and, by construction, enforces conservation laws. In the framework, we are using, unstructured body-fitted meshes with a collocated cell-centered variable arrangement. A formally second-order-accurate method is used for advancing the spatially discretized equations; the time integration is performed using a backward difference scheme. The PIMPLE algorithm, which is a combination of the PISO [66] (Pressure Implicit with Splitting of Operator) and the SIMPLE [67] (Semi-Implicit Method for Pressure-Linked Equations) algorithms are used to ensure pressure-velocity coupling while solving for incompressible flow.

3.3.2 Lagrangian Solver Description

The Lagrangian equation for the dispersed phase given by Eq. (3.1.2) is advanced in time using the first-order-accurate Euler scheme where the source terms are treated implicitly. The dispersed phase's evolution is performed using the enhanced version of the computationally efficient and robust particle tracking algorithm [68]. For example, new position of the particle $\boldsymbol{x}_p^{n+1}$ is computed from the velocity of the particle at the previous time step $v_{\mathrm{p}i}^n$ through

$$x_{\mathrm{p}i}^{n+1} = x_{\mathrm{p}i}^n + v_{\mathrm{p}i}^n \Delta t_p. \tag{3.3.1}$$

Here, the time step size Δt_p can be different from the flow time step as the particles are tracked from cell to cell by calculating and identifying the face crossings. The face crossing approach is more efficient in the tracking of particles in complex geometries of unstructured, arbitrary polyhedral cells, compared to methods that redetermine the hosting grid cell in every iteration. Therefore a series of individual tracking events can be performed for a flow time step size Δt_f, which ends when the particle crosses a face of a cell or when it arrives at the final destination. The maximum time step used to track a particle is one defined for continuous phase simulation (Δt_f). When the particle reaches a new destination either on a face that has been crossed or at the particle's final destination, the new particle velocity at that point is calculated by integrating Eq. (3.1.2)(b) using the implicit Euler scheme.

CHAPTER 4

DESCRIPTION OF COMPUTATIONAL SETUP

In this chapter, the details of the computational setup and cases considered in this study are discussed. These details include the geometry, the computational mesh, the boundary conditions, a list of all the cases, and the simulation strategy considered in this study. We briefly discuss the configuration of the SimInhale geometry used in the benchmark case[1].

4.1 Geometrical Configuration

The geometry considered in this study corresponds to a truncated portion of the SimInhale benchmark flow configuration [1]. Therefore, for the sake of completeness, first, the SimInhale benchmark configuration is described briefly. Afterward, the details of the truncated geometry are presented.

4.1.1 SimInhale Configuration

The computational framework considered in this work utilizes the SimInhale benchmark case [1]. This realistic geometry shown in Fig. 4.1 comprises the oral cavity, larynx, and tracheobronchial airways down to the 12th generation of branching, where the tree was obtained from the human lung of an adult male followed by performing high-resolution computed tomography (HRCT) [69]. HRCT was performed on a rubber cast model based on an adult male's inflated human lung excised at autopsy with the lung tissue and the bones

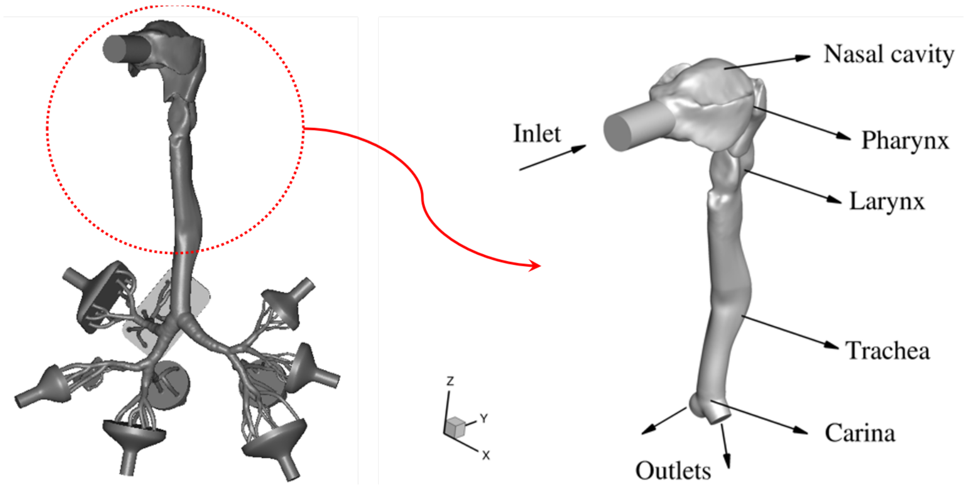

Figure 4.1 The full geometry corresponding to the SimInhale benchmark case (left) and the truncated geometry (right) considered in the present study

removed [69]. While the extrathoracic airways correspond to an upper airway model, which was obtained from the Lovelace Respiratory Research Institute (LRRI), the oral cavity corresponds to an *in vivo* dental impression of a Caucasian male at approximately 50% of the full opening. In contrast, the remaining model was obtained from a cadaver [70]. The geometry obtained from the Lovelace Respiratory Research Institute (LRRI) was a wax cast, which was scanned using Atos device and then converted to STL format and concatenated with the bronchial tree model at trachea [1]. A detailed description of the construction of the airway model is provided elsewhere [71]. This configuration has been used to perform *in vitro* measurements of aerosol deposition at different sections which we would use for verification and validation purposes. The experimental study was performed at steady-state inhalation with three different flow rates (15, 30, and 60 L/min) and two different median sizes of particles (2.5 mm and 4.3 mm). The deposition in different sections was obtained using computed tomography (CT) and positron emission tomography (PET) images from a PET-CT scanner.

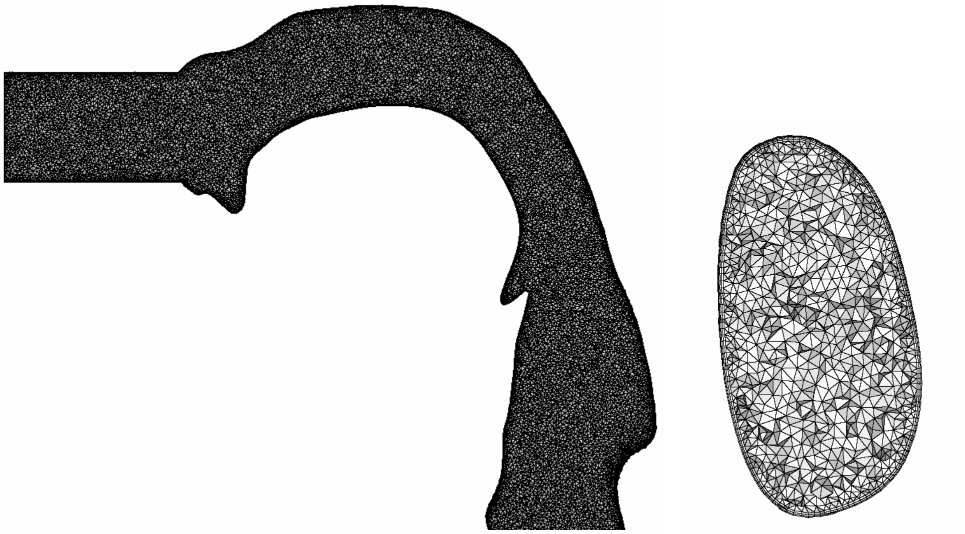

(a) (b)

Figure 4.2 The computational mesh in the central $y-z$ plane of the upper geometry (a) and the cross-sectional plane in the trachea region (b)

To get the edges of the sections' precise location, the CT images are useful, whereas to find the aerosol deposition, positron emission tomography (PET) images were used. Apart from the regional deposition, airflow data at different sections are available, which is being used to assess the numerical methods and models and the employed grid in the present study. A detailed description of the procedure to obtain the SimInhale configuration is provided by Lizal et al. [72].

4.1.2 Truncated Geometry

In the present study, a truncated model of the full geometry (see Fig. 4.1) is considered to examine the airflow and aerosol dynamics in the upper airways. The truncated geometry comprises the extrathoracic and a part of the intrathoracic airways, including carina and left and right main bronchus. The flow within the upper airways exhibits a wide range of variation with several complex flow features such as laminar-to-turbulent transition, shear layers, separation, etc. Such flow features significantly affect the aerosol dynamics primarily due to the inertial impaction and the dispersion mechanisms. Furthermore, the geometrical complexity associated with the bronchial generations can be eliminated to make the computation and the assessment of the computational framework tractable. Due to these reasons, the truncated geometry has been considered in this study. Note that several of the past studies [73] have employed a hybrid 3D/1D approach, where the 3D flow is simulated only in the upper airways, and a 1D network model-based approach is used for the bronchial airways for computational efficiency. The use of truncated geometry allows performing several simulations to examine the capabilities of different modeling strategies in predicting the flow and aerosol dynamics in the regions where a significant portion of the deposition occurs, particularly for the large-sized particles.

4.2 Computational Mesh

The computational domain is spatially discretized using an unstructured mesh comprising of tetrahedral elements in the interior of the domain and prism layers adjacent to the wall (see Fig. 4.2). The prism layers are used in the near-wall region to ensure better control on the near-wall grid resolution to capture the near-wall dynamics. This study considers two computational meshes to examine the behavior of the statistical features of the airflow and aerosol evolution. Table 4.1 summarizes vital statistics of the two grids considered in this study, which include the volume of the computational cell V_{cell}, the height of the cell adjacent to the wall Δr, the average expansion ratio of the prism layers (λ), and near-wall

Table 4.1 Key statistics of the two computational meshes considered in this study

Mesh	Baseline	Fine
$\Delta r_{min}(mm)$	0.09	0.07
Prism Layers	3	3
λ	1.5	1.3
Number of cells ($\times 10^6$)	1.6	6
$(V_{\text{c,min}},\ V_{\text{c,avg}},\ V_{\text{c,max}})(mm^3)$	(0.0004, 0.062, 0.22)	(0.0003, 0.02, 0.21)
y^+_{avg}	0.2	0.8

resolution in terms of y^+. The total number of computational cells in the two meshes are 1.6 M and 6 M, respectively. Both the meshes have a near-wall resolution of less than 1 in wall-units, and therefore, the LES cases correspond to wall-resolved Large Eddy Simulation (LES) in this study.

4.3 Description of Cases

A total of five cases have been simulated in this study to perform the V&V study, assessing the role of grid resolution and the subgrid models for the SGS stress, and finally to examine the effects of Re and d_{p} on the airflow and the particle deposition statistics. Table 4.2 summarizes all the cases considered in this study. Here, $Re = \dfrac{U_{\text{in}} D_{\text{in}}}{\nu}$ is the inlet Reynolds number with U_{in}, D_{in}, and ν denoting bulk velocity at the inlet boundary, the inlet diameter and the kinematic viscosity, respectively. The Stokes number $St_{\text{ref}} = \dfrac{\tau_{\text{p}}}{\tau_{\text{f}}}$ where

Table 4.2 Details of simulations considered in this study

Case	Re	$St_{\mathrm{ref}} \times 10^2$	Mesh size	SGS model
A^{S}	1000	0.01 – 1	1.6 M	SM
B^{L}	3745	0.05 – 5	1.6 M	LDKM
B^{S}	3745	0.05 – 5	1.6 M	SM
BF^{L}	3745	0.05 – 5	6.0 M	LDKM
C^{S}	5000	0.06 – 6	1.6 M	SM

$\tau_{\mathrm{p}} = \dfrac{\rho_p d_p^2}{18\nu\rho}$ is the particle response time and $\tau_f = D_{\mathrm{in}}/U_{\mathrm{in}}$ is the characteristic time scale of the flow.

In all the cases considered here, a uniform velocity profile is specified at the inflow boundary, which is superimposed with 10% turbulence intensity. At the outlet boundary, the mass flow rate is specified to be constant. However, the mass flowrate at the right and the left outlet boundaries is specified to be 71%, and 29% of the total inlet mass flow rate to account for the observed high asymmetry for the airflow in the experiments [1, 71]. The no-slip boundary condition is imposed on all the airway walls.

To examine the effects of Re, three cases labeled as 'A', 'B' and 'C' with $Re = 1000$, 3745, and 5000, respectively (see Table 4.2), are simulated. These values of Re are considered to demonstrate the effects of transitional behavior of the flow on the airflow and the particle statistics. The evolution of particles with different values of d_{p} is examined by considering seven different values of d_{p} of 1, 2, 2.5, 4.3, 6, 8, and 10 μm, which leads to a variation from 0.01 to 6 for the Stokes number in different cases. As stated in Sec 3.1, one-way coupled particle-laden flow is considered where the airflow affects the evolution of particles, but particles do not affect the airflow. Also, the forces resulting from only drag and gravity are considered during the particles' evolution, and all particle-to-particle interactions are neglected. Furthermore, the particles approaching the wall sticks to the wall, whereas they can exit out of the domain through the outlet boundary.

A key focus of the study is on the assessment of closure models for the SGS stress. To address this, two widely-popular closures for SGS stress, namely the Smagorinsky eddy viscosity model (SM) [33], and the locally dynamic kinetic energy model (LDKM) [34] are considered. The cases are labeled with superscript 'S' and 'L' for the SM and LDKM models. The description of these closure models is provided in Sec. 3.2. Finally, an additional case labeled as '$\mathrm{BF}_{\mathrm{S}}^{\mathrm{L}}$' is simulated to examine the effects of the grid resolution.

All the simulations are first evolved for 2 flow-through times (T_{f}). Here, $T_{\mathrm{f}} = L_{\mathrm{c}}/U_{\mathrm{in}}$ with L_{c} is a representative length of the domain along the direction of the mean flow. Afterward, turbulence statistics are gathered for running the simulations for an additional 2 flow through time, and computing the running average of the flow quantities. With the evolved flow field, 100,000 particles with seven different values of d_p are injected at the rate of 40000 particles per second for 0.025 seconds, and the simulation is carried out till the global deposition of the particles reaches a quasi-stationary state.

All the simulations are carried out in parallel using the message passing interface (MPI) library. The computational cost of the cases employing LDKM is about 30% more than the cases using SM for the SGS stress closure. This is due to the need to solve an additional transport equation for the SGS kinetic energy (k^{sgs}) while using the LDKM for the closure of the SGS stress. As expected, the cost of the fine-mesh case is higher compared to the coarse mesh case. In particular, the cost of the fine mesh case is about 1.5 times the cost of the baseline mesh case.

CHAPTER 5

ASSESSMENT OF COMPUTATIONAL FRAMEWORK

In this chapter, we focus on case B ($Re = 3745$) to examine the performance of the computational modeling strategy. We compare the airflow results against the reference experimental and numerical results [1]. The reference numerical results correspond to the LES of the entire SimInhale geometry using a very fine mesh comprising of 50 M computational cells. The subgrid scale model used in the reference numerical results was Dynamic Smagorinsky. First, we analyze the results for airflow, and then we assess the accuracy of the results for the global and the local aerosol deposition by comparing the Deposition Fraction ($D_F(\%)$). Finally, we analyze the role of grid refinement on the global deposition characteristics.

5.1 Comparison of Airflow

The comparison of the airflow prediction is performed in the term of time-averaged (mean) velocity magnitude profile extracted at six different cross-sectional locations within the airway geometry. These locations are shown in Fig. 5.1 where contours of the mean velocity magnitude ($|\langle \widetilde{\boldsymbol{u}} \rangle|$) are shown in the central $y-z$ plane. We can observe a significant variation of $|\langle \widetilde{\boldsymbol{u}} \rangle|$ along the airway geometry, which is expected due to the complexity of the geometry and rapid changes in the flow direction. In particular, we can observe the presence of shear layers, asymmetric distribution of the flow in the cross-sectional planes,

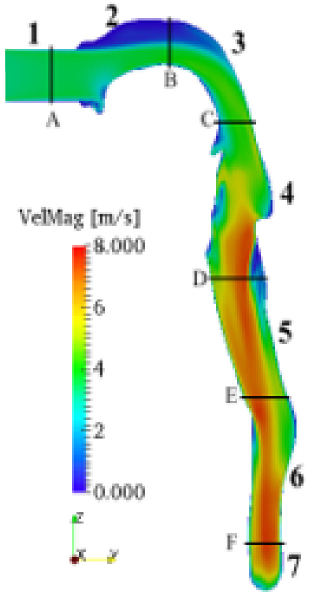

Figure 5.1 Contour of mean velocity magnitude ($|\langle\widetilde{\boldsymbol{u}}\rangle|$) in central $y-z$ plane with cross-sectional locations identified (A through F) where profiles are extracted

flow acceleration, separation/reattachment, etc. The presence of such features significantly affects aerosol deposition, which is discussed later.

Figure 5.2 shows comparison of the profiles of $|\langle\overline{\boldsymbol{u}}\rangle|$ obtained using LDKM and SM cases with respect to the reference LES results [1] extracted at six different cross-sectional locations. Overall, we can observe a reasonable agreement in the results from the cases simulated in this study against the reference case. The agreement improves in the later sections of the airways, with significant differences occurring near the inlet sections, particularly at section A-A. This can be attributed to a difference in the inlet velocity boundary conditions used in the current study compared to the reference study. In our cases, we employ a constant velocity inlet with imposed turbulent fluctuations, whereas in the reference case, an auxiliary simulation is performed to specify a fully developed turbulent inlet velocity pro-

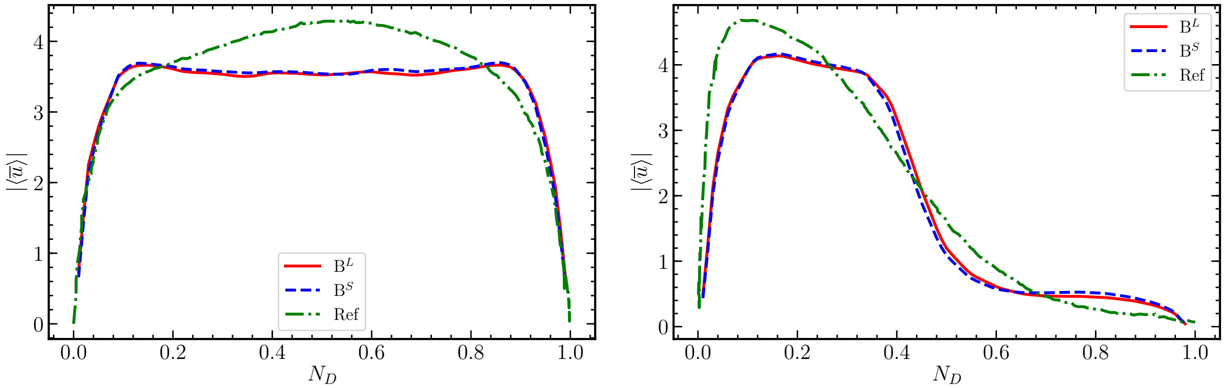

(a) A-A

(b) B-B

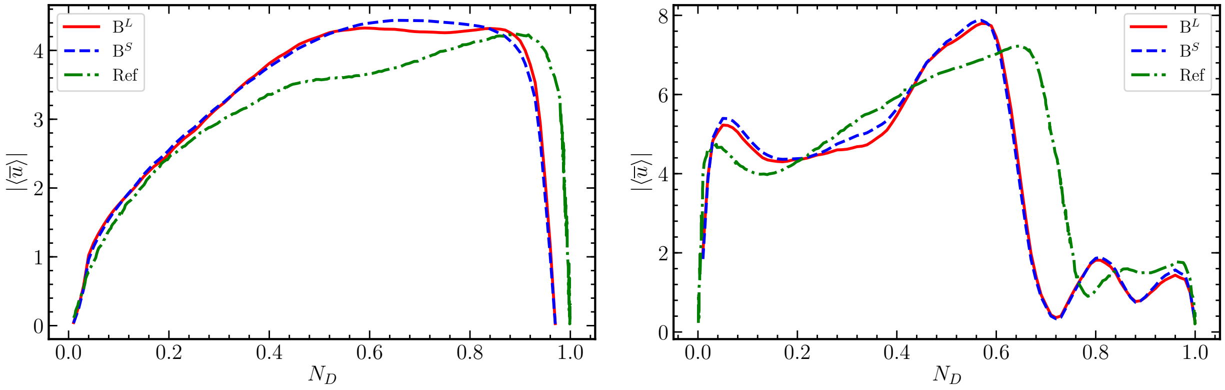

(c) C-C

(d) D-D

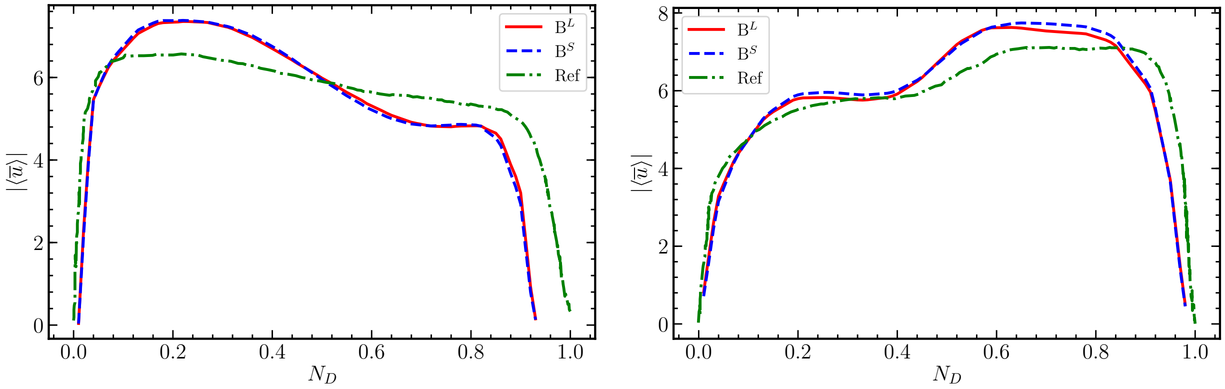

(e) E-E

(f) F-F

Figure 5.2 Comparison of profiles of the mean velocity magnitude ($|\langle\widetilde{\boldsymbol{u}}\rangle|$) at six different cross-sectional locations obtained using DEVM and LDKM cases with respect to the reference LES results [1] file. Note that in the nasal cavity region, i.e., in the vicinity of section B-B, the flow field changes abruptly due to the underlying geometrical changes, which in low *Re* flows leads to transition-to-turbulence behavior. Therefore, the effects of inlet velocity boundary conditions reduce beyond this region, which is apparent from a better agreement of the results at section B-B and at the further downstream sections.

A key feature of the flow is the presence of asymmetrical behavior as evident in Fig. 5.1, which is also evident in profiles at all the locations except at section A-A, which is close to the inlet. At section B-B, located at the center of the nasal cavity, a large separated flow region is observed (see Fig. 5.1). This manifests into a reduced magnitude of the velocity field in the vicinity of the upper portion of the nasal cavity. At section C-C, located in the upper part of the pharynx, the effect of bending of the flow is evident in the form of the higher values observed in the vicinity of the posterior wall. At section D-D, located immediately below the larynx, the glottal constriction in the airway accelerates the flow causing an enhanced mean velocity magnitude in the core region of the airway. The curvature of the airway leads to the formation of shear layers. The sections E-E and F-F are located above the trachea and at the Carina, respectively. We observe a transition of the location of the peak velocity magnitude from the anterior to the posterior walls.

Both SM and LDKM cases can capture the mean flow statistics within the airways in good agreement with the reference results, thus illustrating the employed computational framework's ability to capture the mean flow variations. Furthermore, we notice only minor differences in the results from the cases employing SM and the LDKM for the closure of the subgrid-scale (SGS) stress, thus demonstrating that either of the subgrid-scale (SGS) closure models can be used for modeling the airflow. However, further investigations are needed to examine the behavior of the second-order turbulence statistics while using these closure models.

5.2 Comparison of Aerosol Deposition

For the SimInhale benchmark case, we have reference numerical results available for global and regional aerosol deposition at $Re = 3745$ for several discrete particle sizes, and *in vitro* measurements are also available for the same flow conditions for the particle size of 4.3 μm. We use these reference results to perform the verification and validation (V&V) of the computational modeling strategy. The aerosol deposition is affected by the inertial impaction, gravitational sedimentation, interception, and the turbulence dispersion [74], but in the upper airway region, the aerosol deposition is primarily affected by two key mechanisms, namely, the inertial impaction and the turbulence dispersion. The inertial impaction occurs when the particle has sufficient momentum and cannot follow the flow field [75]. Essentially, the larger particles are more influenced by inertial impaction than the smaller particles due to their inertia. The other mechanism, which affects the deposition characteristics in a turbulent flow field, is the turbulent dispersion of the particles. It occurs due to the irregular mixing of fluid in the turbulent regime, due to which the fluid speed and the trajectory of a particle changes, leading to the eventual deposition on the airway walls [74]. In particular, the smaller particles tend to be more influenced by turbulence dispersion than the larger particles. In the present study, the particles that are stuck to the geometry walls are considered to be deposited. For discrete particle sizes, the $D_F(\%)$ is

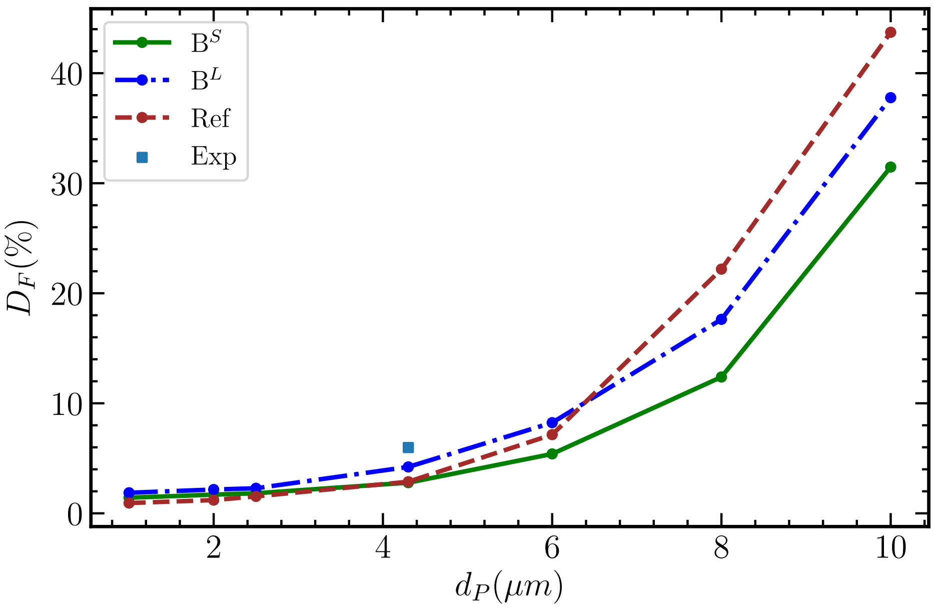

Figure 5.3 Comparison of global deposition fraction as a function of the particle size for $Re = 3745$ case

calculated across the entire geometry for global deposition. The $D_F(\%)$ is calculated as a ratio of the number of particles stuck to the wall and the number of particles injected at the inlet boundary.

Fig. 5.3 shows the global D_F as a function of d_p for case B. The results obtained from cases B^S and B^L differ in the type of the SGS model and are compared with the reference LES and *in vitro* results. We observe that the deposition fraction increases with an increase in d_p, showing that inertial impaction is the more dominant deposition mechanism in the upper airways. The deposition fraction for the particle size less than 5 μm is small($D_F <$ 7%), which shows that turbulence dispersion does not affect the deposition as much as inertial impaction. We can also observe a large variability in the value of D_F with the increase in the value of d_p (D_F increases by 5 to 6 times). Here, we observe that the case employing

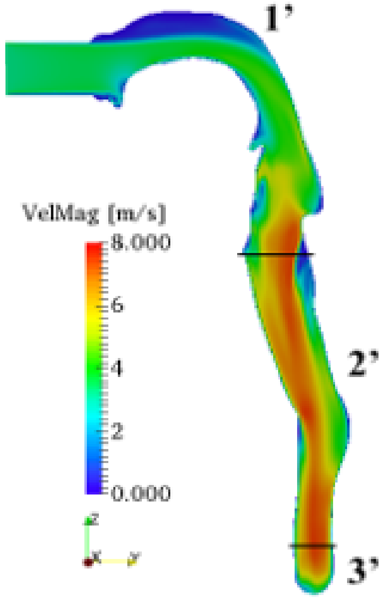

Figure 5.4 Contour of velocity magnitude with segments for deposition

LDKM shows marginally better agreement with the reference results compared to the case when SM is used for closure of the subgrid scale (SGS) stress. Note that, in the LDKM, an additional transport equation is solved for the SGS kinetic energy, which in turn is used to obtain the eddy viscosity (see Eq. (3.2.5)). However, the predictions by the SM based closure can be considered reasonable as it can capture all the trends, and is, therefore, used for further investigation of the effects of Re on the global and local variation of D_{F} with respect to d_{p}.

For a more detailed assessment of the employed computational modeling strategy, we analyze the local deposition characteristics now. We divide the upper airway geometry into three segments to perform this analysis, as seen in Fig. 5.4. The first segment corresponds to the section of the airway from the inlet to the larynx region. The second segment includes the region below the larynx up to the trachea. The last segment corresponds to the region from the carina to the outlets.

Fig. 5.5 compares the local value of D_{F} obtained using the SM and LDKM closures with the reference data at different segments for different particle sizes. We observe a large variability in the regional deposition fraction with respect to d_{p}, which is consistent with the global value of D_{F} shown in Fig. 5.3. We can notice a significant increase in the deposition with the increase in particle size in all three segments. The D_F increases by 5 to 6 times for particle sizes greater than 5 μm.

The variation of local deposition is consistent for all the particle sizes, where we observe the highest deposition in the first segment, which reduces in the second segment, followed by an increase in the last segment. This trend is captured by both the closures in a manner consistent with the reference results. For the particle sizes of d_{p} =1 μm and 2.5 μm, both the cases show a marginal overprediction in the regional deposition. However, for higher values of d_{p}, an under-prediction is observed. Overall, similar to the global deposition, the case employing the LDKM closure shows a marginally better prediction than the case using the SM closure, particularly for higher values of d_{p}. Furthermore, for large-size particles, the differences with respect to the reference case are large, as for such particles, Stokes number is high, which leads to an increase in the particle evolution's sensitivity to the flow field.

5.3 Grid Sensitivity Study

In Secs. 5.1 and 5.2, we showed that the computational modeling strategy considered in this study with the baseline grid of 1.6 M computational cells can capture the mean flow

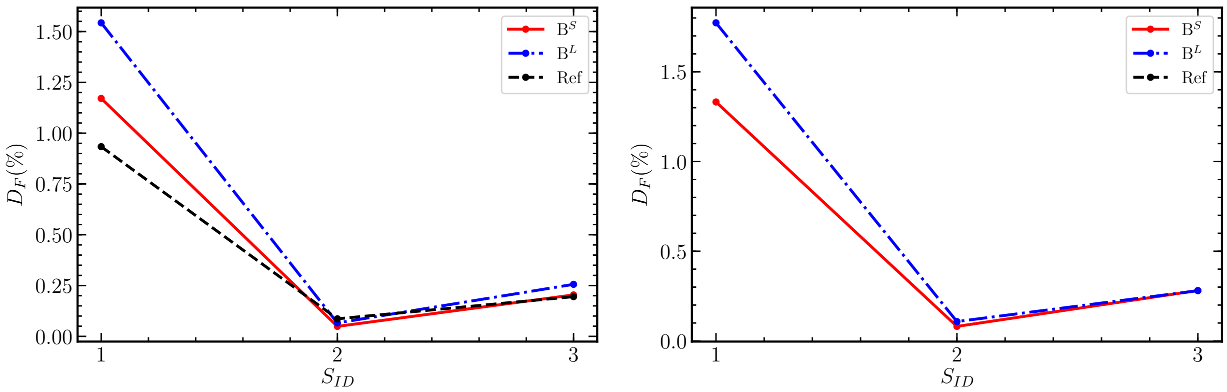

(a) $d_\mathrm{p} = 1\ \mu\mathrm{m}$ (b) $d_\mathrm{p} = 2\ \mu\mathrm{m}$

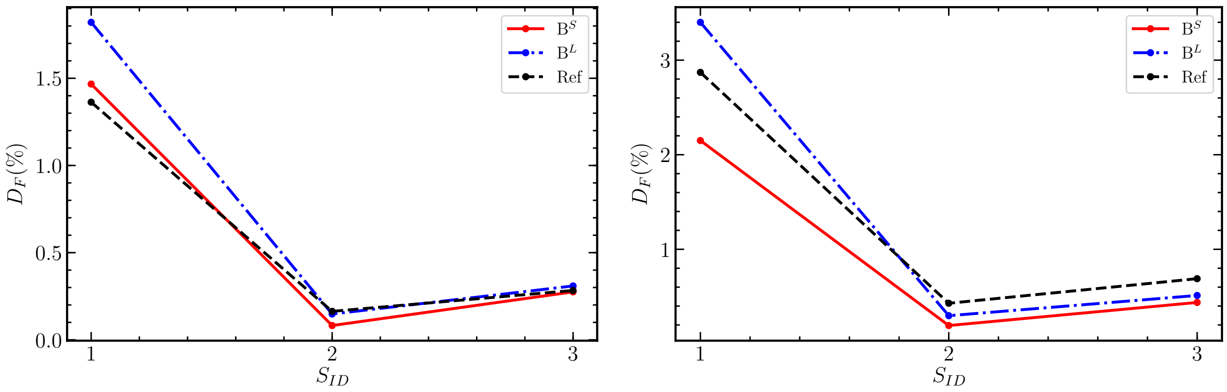

(c) $d_\mathrm{p} = 2.5\ \mu\mathrm{m}$ (d) $d_\mathrm{p} = 4.3\ \mu\mathrm{m}$

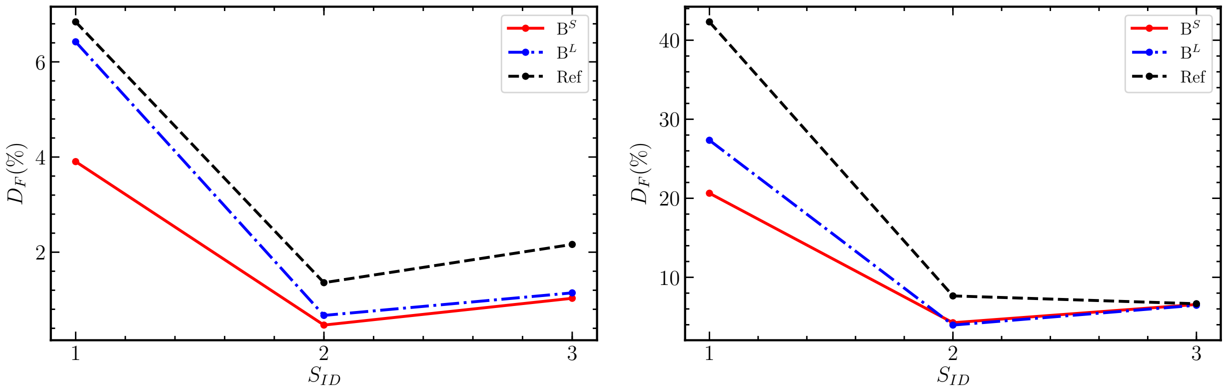

(e) $d_\mathrm{p} = 6\ \mu\mathrm{m}$ (f) $d_\mathrm{p} = 10\ \mu\mathrm{m}$

Figure 5.5 Region deposition fraction (D_F) in the airway geometry for particles of different sizes (1-10 μm)

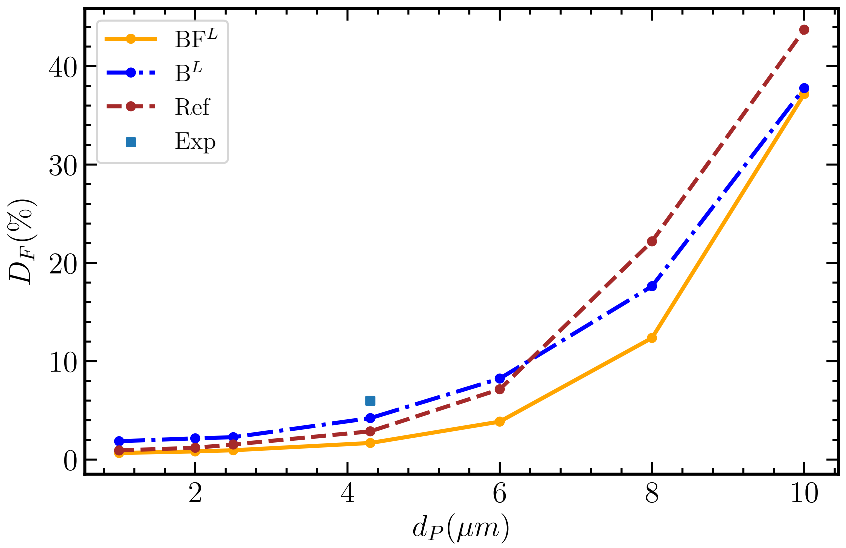

Figure 5.6 Comparison of the global deposition fraction obtained using two different mesh and compared with respect to the reference case

and the aerosol deposition characteristics in good agreement with the reference results. Now, we examine the role of the grid resolution on the prediction of the global deposition.

Compared to the baseline mesh, the fine grid mesh comprises approximately 6 M cells. Fig. 5.6 compares the global deposition fraction for the cases using two different computational mesh with the reference data for different particle sizes. Overall, with both meshes, we obtain a similar variation of the global deposition fraction with respect to the particle size, thus demonstrating the baseline grid's adequacy. In particular, for $d_\mathrm{p} \lessapprox 5$ μm, the fine grid case shows marginally better results than the baseline grid case. However, for $d_\mathrm{p} = 6$ and 8 μm, we observe that the baseline grid shows a better agreement with the reference data while for $d_\mathrm{p} = 10$ μm, both cases show similar results. The observed differences with the reference results and between the two cases can be attributed to the role of subgrid dispersion, which is neglected in the present study.

CHAPTER 6

EFFECTS OF REYNOLDS NUMBER

In this chapter, we assess the effects of Reynolds Number (Re) on the statistics of the airflow and the aerosol deposition. As mentioned in Sec. 4.3, we have considered three different values of Re (1000, 3745, and 5000) to analyze the effect of low (1000) and high (5000) Re compared to the reference case with $Re = 3745$. Here, $Re = 1000$ is considered because for this value of Re, the flow exhibits quasi-laminar characteristics near the inlet region of the computational domain, whereas $Re = 5000$ has fully developed turbulent characteristics. First, we assess the effect of Re on the first-order statistics of the airflow, and then we analyze the effects on the deposition characteristics.

6.1 Effects of Re on Airflow

The instantaneous coherent vortical structures reveal the physical characteristics and dynamics of the flow field. These structures are responsible for the production and transport of the turbulent kinetic energy [76] and can be identified using the second invariant of the velocity gradient tensor denoted by Q [2], which is defined as

$$Q = \frac{1}{2}\left(\Omega_{ij}\Omega_{ij} - S_{ij}S_{ij}\right), \tag{6.1.1}$$

Where S_{ij} and Ω_{ij} are strain- and rotation-rate tensors, respectively. Figure 6.1

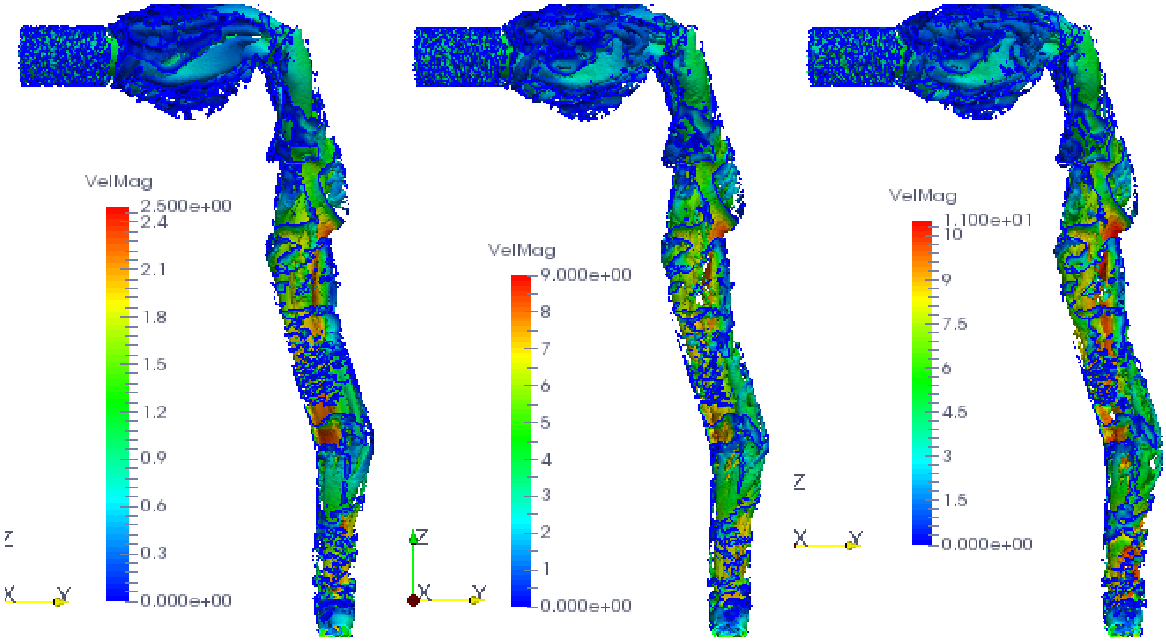

(a) $Re = 1000$ (b) $Re = 3745$ (c) $Re = 5000$

Figure 6.1 Instantaneous vortical structures in the three cases identified using the iso-surface of Q-criterion [2] and colored by the instantaneous velocity magnitude

shows the vortical structures identified using a positive value of Q for all three cases and colored by the corresponding instantaneous velocity magnitude. A wide range of flow structures tends to form in all the cases, which starts particularly in the nasal cavity region. The intense shear layer is evident within the larynx, pharynx, and trachea regions. The effects of Re is particularly evident between the $Re = 1000$ and 5000 cases, with $Re = 3745$ case exhibiting a behavior similar to the $Re = 5000$ case. The difference between the low and the high Re cases is evident in terms of the appearance of fine-grained structures in the regions past the nasal cavity in the high Re case. The complexity of the flow is also evident in all three cases thus demonstrating the observed variation of the aerosol deposition in different segments as discussed in chapter 5.

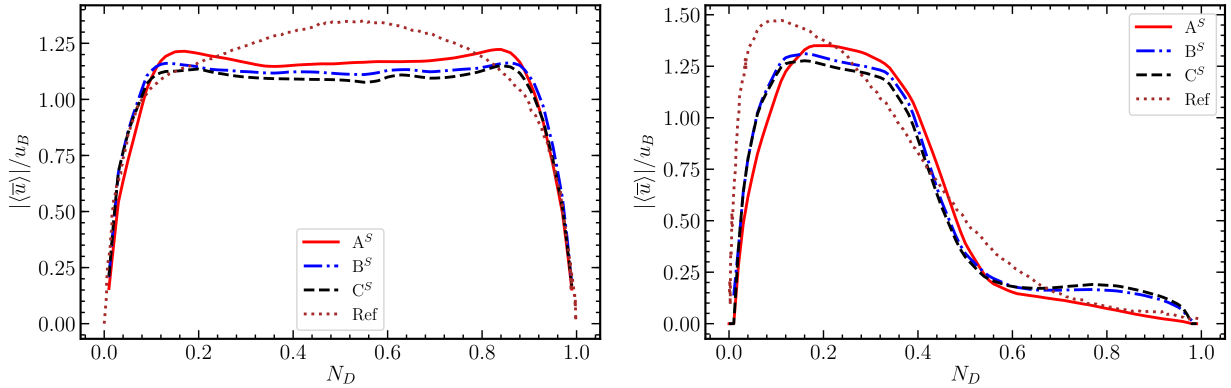

(a) A-A (b) B-B

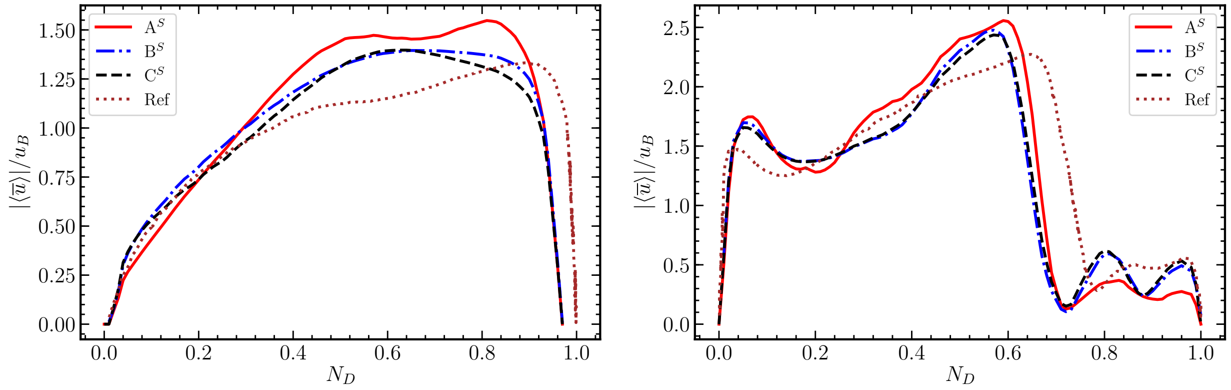

(c) C-C (d) D-D

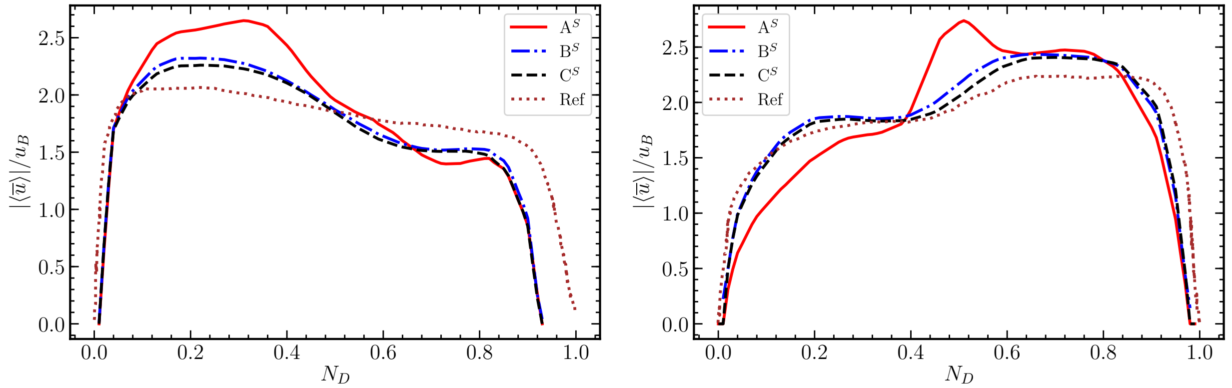

(e) E-E (f) F-F

Figure 6.2 Profile of the mean velocity magnitude at different cross sections for different values of Reynolds number (Re). The reference results correspond to a fine-grid LES [1] at $Re = 3745$

Fig. 6.2 shows profiles of the normalized mean velocity magnitude ($|\langle\tilde{u}\rangle|/u_{\mathrm{B}}$) at different cross sections as seen in Fig. 5.1. We can observe asymmetric profiles of $|\langle\tilde{u}\rangle|/u_{\mathrm{B}}$ at different cross sections, except cross-section A-A in all cases. In particular, at cross-section A-A, we observe that the effects of Re are marginal, with case A^{S} exhibiting slightly higher values. At cross-section B-B, the effects of Re is apparent, and in all cases a significant asymmetry is prevalent. The difference between high Re cases, i.e., case B^{S} and case C^{S} is much smaller compared to that with respect to case A^{S}.

At cross-section C-C, which corresponds to the larynx region, the effects of Re are much more apparent, where the peak location of the velocity magnitude shifts to the posterior airway region. The peak value is sharper in the low Re case compared to the other two cases. The shift in the peak location is due to the bend in the trachea region. We observe that all three cases exhibit a very similar behavior at cross-section D-D below the larynx region except in the posterior wall region.

At cross-sections E-E and F-F, the effects of Re again get pronounced, where the low Re case differs significantly from the other two and the reference cases. Notably, at cross-section E-E, due to the bend in the trachea region, the high-speed flow moves towards the anterior region from the posterior wall. However, we observe that in the low Re case, the velocity magnitude near the anterior wall increases comparatively higher than the other high Re cases. Finally, at the cross-section F-F, the flow at the anterior end decreases much more in the low Re case than the high Re cases, and we also observe a sudden increase in velocity magnitude in the core region in this case.

Overall, a summary of the mean flow characteristics for different values of Re as shown in Fig. 6.2 are given below:

- The case at low Reynolds number Re shows significant differences with the other two values of Re because this particular Re flow exhibits a transitional behavior. The normalized velocity magnitude profiles from the other two high Re cases show a near collapse at all the cross-sections due to fully developed turbulence conditions in these cases.
- The low Re case shows little or no variation till the flow reaches the larynx when the flow characteristics change to a fully developed turbulent flow. It shows that the inflow conditions do not have a significant effect after the larynx region.
- The profiles of the normalized velocity magnitude from the two high Re cases exhibit a good agreement with the reference LES results.

These results indicate that the aerosol deposition characteristic will be, as expected, Re dependent apart from St_{ref} dependent. This aspect of the global and local deposition characteristics is examined next.

6.2 Effect of Re on Aerosol Deposition

The effects of Reynolds number Re on the variation of the global deposition fraction (D_{F}) with respect to the particle size (d_{p}) is shown in Fig. 6.3. We can observe that with an increase in Re, the value of Deposition Fraction D_{F} remains largely unaffected for particle size less than 5 μm, which can be attributed to an insignificant effect of turbulent fluctuations on the deposition of the smaller size particles. However, for larger particles size, i.e., for $d_{\mathrm{p}} > 5$ μm, we observe that with an increase in d_{p}, D_{F} increases and the increase

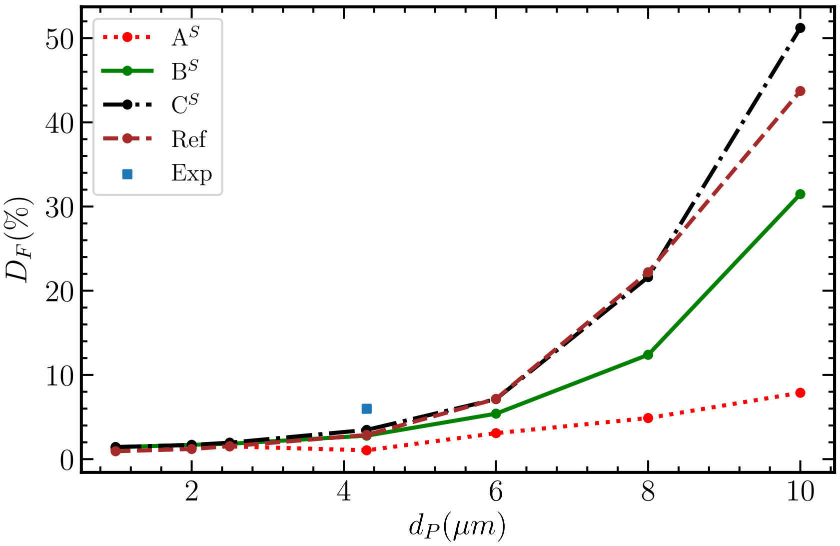

Figure 6.3 Deposition fraction as a function of particle size comparing different Reynolds number

is higher as Re is increased. Such a variation of D_{F} with d_{p} has been observed in Fig. 5.3. With the increase in Re, the effect of inertial impaction is more significant than turbulence fluctuations as we observe deviation in the deposition results primarily for the larger size particles.

Fig. 6.4 shows the regional deposition fraction across different segments for the six particle sizes comparing the three different Reynolds number values. Similar to the global deposition for smaller size particles as shown in Fig. 6.3, we can observe in Fig. 6.4(a)-(c) that for particle size less than 5 μm, the effect of Re on the local deposition is minimal. However, with an increase in the particle size d_{p}, we start to observe differences in the local deposition as Re is increased. In particular, for particle size greater than 5 μm at cross-sections D-D, E-E, and F-F, the increase in deposition across the entire airway geometry occurs. Similar to the variation of the global deposition, the effects of Re is much more apparent for larger

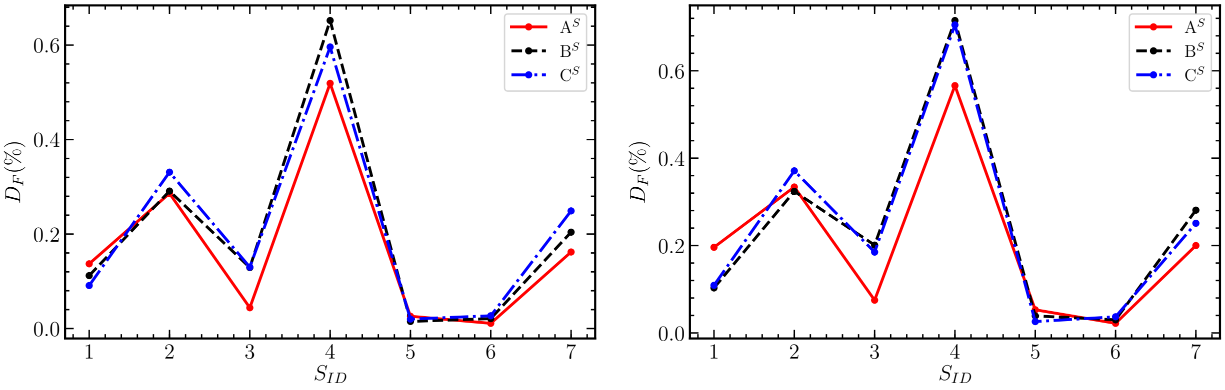

(a) $d_\mathrm{p} = 1\ \mu$m (b) $d_\mathrm{p} = 2\ \mu$m

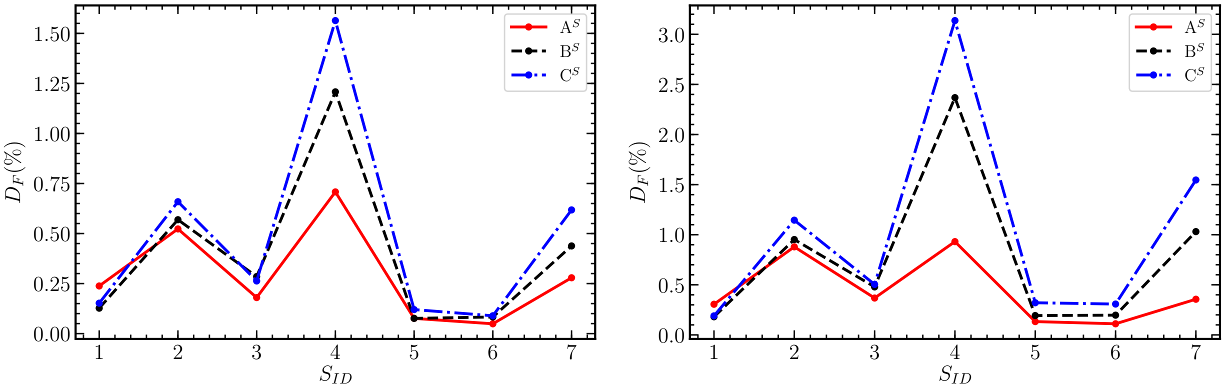

(c) $d_\mathrm{p} = 4.3\ \mu$m (d) $d_\mathrm{p} = 6\ \mu$m

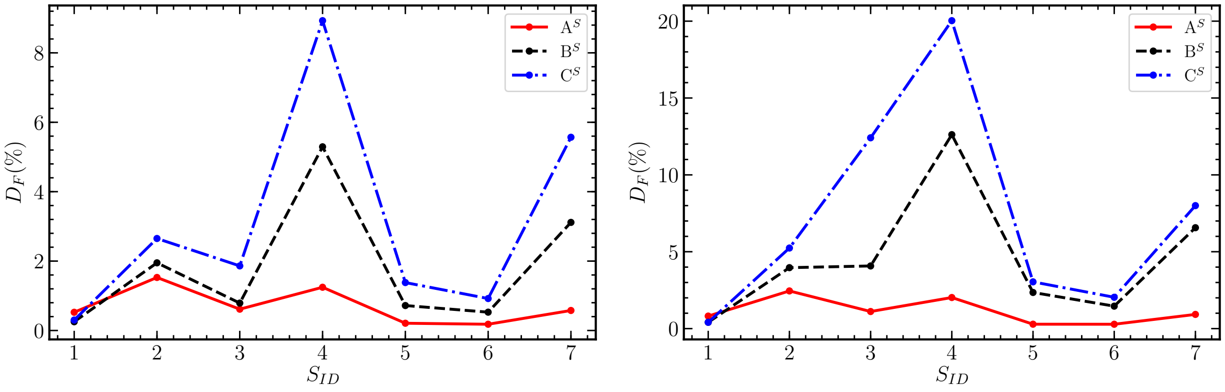

(e) $d_\mathrm{p} = 8\ \mu$m (f) $d_\mathrm{p} = 10\ \mu$m

Figure 6.4 Deposition Fraction at various segments comparing different Reynolds number particle size. Overall, for all the particle sizes considered in this study, the largest deposition occurs at section 4, which corresponds to the region between the pharynx and larynx. The effect of *Re* on the local deposition is also significant in this region. Note that while the smaller particles show higher deposition in the nasal cavity, larynx, and outlet regions, the larger particles show higher local deposition near the larynx and the outlet regions.

The dependence of the regional deposition characteristics described here as a function of *Re*, i.e., the inlet mass flow rate and the particle size d_p can be used to guide the specification of aerosolized drug delivery for the treatment of pulmonary ailments. In particular, the predictive computational tool employed in this study can be used to estimate the parameters of the inhaler-based therapy for curing regional issues within the airways, which can maximize the efficiency and minimize the side effects of the prescribed medication.

CHAPTER 7

CONCLUSIONS

In this chapter, first, the key accomplishments of this study are highlighted in terms of the critical technical objectives described in Sec. 1.1, and then the future scope of the present work is outlined.

7.1 Key Accomplishments

The specific accomplishments of this thesis are as follows:

- **Assessment of modeling strategy:** In this study, the capabilities of the computational framework to carry out Large-Eddy Simulation(LES) of particle-laden flow within the human airways using the Eulerian-Lagrangian framework has been established. This is achieved by simulating cases corresponding to a truncated geometry of the well-established SimInhale benchmark configuration and comparing the results for the mean flow and local and global deposition of particles in the upper airway. We have assessed the performance of two SGS closure models, namely, the algebraic SM and the one-equation-based LDKM. Overall, similar results were obtained through both methods for the mean flow, but slightly better results were obtained by the the one-equation-based LDKM for the aerosol deposition. The reason for better results with the LDKM method can be attributed to the solution of an additional transport equation for the subgrid kinetic energy, which is used to obtain the eddy viscosity for the closure of the SGS stress. However, LDKM also tends to be computationally expensive by around 30% for the cases considered in this study due to the need to solve an additional transport equation.

- **Analyze the airflow statistics:** The mean flow statistics have been assessed by adopting different closure models, three sets of Reynolds numbers, and different mesh sizes. A reasonable comparison was found with the reference data. We observe the flow to be quasi-laminar near the inlet boundary, and it transitions to turbulence at the back of the nasal cavity. The velocity magnitude is low at the inlet up to the pharynx, and it accelerates near the larynx. The low Reynolds number flow shows little to no variation until the flow reaches the larynx, after which the inflow conditions do not show a significant effect on the mean flow field.
- **Characterize the effects of injection flow rate and particle size:** As stated above, we compared the deposition characteristics of particles with different sizes (Stokes number) for three different values of Reynolds numbers to study the effects of injection flow rate and particle size. For airflow, we observed that $Re = 3745$ and 5000 cases show the collapse of normalized mean velocity magnitude while the low Re flow differs; this is due to the transitional nature of the flow at lower Re. We also observe that for aerosol deposition, the smaller particle size (less than 5μm) deposition is largely unaffected while for particle size greater than 5 μm Re has significant effects on the deposition characteristics. Finally, as expected, a higher Re leads to enhanced inertial impaction, which in turn increases the deposition, particularly for the particles with a higher Stokes number.

7.2 Future Outlook

Some of the directions that one can pursue to extend this research activity in the future are summarized below:

- **Improve upon predictive capabilities of the computational strategy**: The computational framework considered here neglects the subgrid dispersion, which is important, particularly while using a coarse grid for LES (Large-Eddy Simulation). So, a future study can focus on examining the results with different models for subgrid dispersion. In addition, other closure models for the Subgrid scale (SGS) stress can also be assessed for their accuracy and efficiency compared to the closures considered in this study. Finally, the two- and four-way coupled particle-laden flow scenarios can also be considered.
- **Examine the deposition characteristics for polydisperse injection:** In this study, we have used seven discrete particle sizes ranging from 1 to 10 μm, but in the future, instead of discrete particle size, a different distribution method can be used. For example, particles can be distributed by Gaussian size distribution or by mean-variance distribution methods at the inlet.
- **Develop correlations for deposition**: We have established a strong dependence of the deposition fraction (D_F) with the Reynolds number and particle size or the Stokes number. These results can be used to develop correlations for the deposition fraction in terms of the non-dimensional parameters.
- **Simulate the full geometry**: In the current study, we have focused on the upper airway geometry. However, one can extend the study to include the entire airway model

from extra-thoracic airway to tracheobronchial airways, which could lead to improved understanding of the deposition characteristics in the peripheral regions, which is key for the treatment of several pulmonary ailments.

REFERENCES

[1] P Koullapis, Stavros C Kassinos, J Muela, C Perez-Segarra, J Rigola, Oriol Lehmkuhl, Y Cui, M Sommerfeld, J Elcner, M Jicha, et al. Regional aerosol deposition in the human airways: The siminhale benchmark case and a critical assessment of in silico methods. *European Journal of Pharmaceutical Sciences*, 113:77–94, 2018.

[2] J. Jeong and F. Hussain. On the identification of a vortex. *J. Fluid Mech.*, 285:69–94, 1995.

[3] Busse WW. Lemanske rf jr. asthma. *N Engl J Med*, 344:350–362, 2001.

[4] Kazuto Matsunaga, Tsunahiko Hirano, Asako Oka, Ayaka Tanaka, Kuninobu Kanai, Takashi Kikuchi, Atsushi Hayata, Hiroaki Akamatsu, Keiichiro Akamatsu, Yasuhiro Koh, et al. Progression of irreversible airflow limitation in asthma: correlation with severe exacerbations. *The Journal of Allergy and Clinical Immunology: In Practice*, 3 (5):759–764, 2015.

[5] World Health Organization et al. *Global surveillance, prevention and control of chronic respiratory diseases: a comprehensive approach*. 2007.

[6] Global Asthama Network. The global asthma report. *Global Asthma Network,Auckland, New Zealand:*, pages 1–92, 2004.

[7] Warren H Finlay. *The mechanics of inhaled pharmaceutical aerosols: an introduction*. Academic press, 2001.

[8] AR McFarland, H Gong, A Muyshondt, WB Wente, and NK Anand. Aerosol deposition in bends with turbulent flow. *Environmental science & technology*, 31(12):3371–3377, 1997.

[9] K_-W Stapleton, E Guentsch, MK Hoskinson, and WH Finlay. On the suitability of k–ε turbulence modeling for aerosol deposition in the mouth and throat: a comparison with experiment. *Journal of Aerosol Science*, 31(6):739–749, 2000.

[10] Clement Kleinstreuer and Zhe Zhang. Laminar-to-turbulent fluid-particle flows in a human airway model. *International Journal of Multiphase Flow*, 29(2):271–289, 2003.

[11] EA Matida, Warren H Finlay, CF Lange, and B Grgic. Improved numerical simulation of aerosol deposition in an idealized mouth–throat. *Journal of Aerosol Science*, 35(1): 1–19, 2004.

[12] M Breuer, HT Baytekin, and EA Matida. Prediction of aerosol deposition in 90^o bends using LES and an efficient Lagrangian tracking method. *Journal of Aerosol Science*, 37 (11):1407–1428, 2006.

[13] Yuan Liu, Edgar A Matida, Junjie Gu, and Matthew R Johnson. Numerical simulation of aerosol deposition in a 3-d human nasal cavity using rans, rans/eim, and les. *Journal of aerosol science*, 38(7):683–700, 2007.

[14] HH Jin, JR Fan, MJ Zeng, and KF Cen. Large eddy simulation of inhaled particle deposition within the human upper respiratory tract. *Journal of Aerosol Science*, 38 (3):257–268, 2007.

[15] ST Jayaraju, M Brouns, S Verbanck, and C Lacor. Fluid flow and particle deposition analysis in a realistic extrathoracic airway model using unstructured grids. *Journal of Aerosol Science*, 38(5):494–508, 2007.

[16] Ching-Long Lin, Merryn H Tawhai, Geoffrey McLennan, and Eric A Hoffman. Characteristics of the turbulent laryngeal jet and its effect on airflow in the human intrathoracic airways. *Respiratory physiology & neurobiology*, 157(2-3):295–309, 2007.

[17] Zheng Li, Clement Kleinstreuer, and Zhe Zhang. Particle deposition in the human tracheobronchial airways due to transient inspiratory flow patterns. *Journal of aerosol science*, 38(6):625–644, 2007.

[18] ST Jayaraju, M Brouns, C Lacor, B Belkassem, and S Verbanck. Large eddy and detached eddy simulations of fluid flow and particle deposition in a human mouth–throat. *Journal of Aerosol Science*, 39(10):862–875, 2008.

[19] Hari Radhakrishnan and Stavros Kassinos. Cfd analysis of turbulent particle deposition in the lungs. In *ASME 2009 Summer Bioengineering Conference*, pages 445–446. American Society of Mechanical Engineers Digital Collection, 2009.

[20] Jan W De Backer, Wim G Vos, Samir C Vinchurkar, Rita Claes, Anton Drollmann, Denis Wulfrank, Paul M Parizel, Paul Germonpré, and Wilfried De Backer. Validation of computational fluid dynamics in ct-based airway models with spect/ct. *Radiology*, 257(3):854–862, 2010.

[21] C Kleinstreuer and Z Zhang. Airflow and particle transport in the human respiratory system. *Annual review of fluid mechanics*, 42:301–334, 2010.

[22] A Dehbi. Prediction of extrathoracic aerosol deposition using rans-random walk and les approaches. *Aerosol Science and Technology*, 45(5):555–569, 2011.

[23] P Worth Longest and Landon T Holbrook. In silico models of aerosol delivery to the respiratory tract—development and applications. *Advanced Drug Delivery Reviews*, 64 (4):296–311, 2012.

[24] L Nicolaou and TA Zaki. Direct numerical simulations of flow in realistic mouth–throat geometries. *Journal of aerosol science*, 57:71–87, 2013.

[25] PG Koullapis, Stavros C Kassinos, Mariya Petrova Bivolarova, and Arsen Krikor Melikov. Particle deposition in a realistic geometry of the human conducting airways: Effects of inlet velocity profile, inhalation flowrate and electrostatic charge. *Journal of biomechanics*, 49(11):2201–2212, 2016.

[26] L Nicolaou and TA Zaki. Characterization of aerosol stokes number in 90^o bends and idealized extrathoracic airways. *Journal of Aerosol Science*, 102:105–127, 2016.

[27] Said Elghobashi. On predicting particle-laden turbulent flows. *Applied scientific research*, 52(4):309–329, 1994.

[28] CT Crowe, TR Troutt, and JN Chung. Numerical models for two-phase turbulent flows. *Annual Review of Fluid Mechanics*, 28(1):11–43, 1996.

[29] S Balachandar and John K Eaton. Turbulent dispersed multiphase flow. *Annual review of fluid mechanics*, 42:111–133, 2010.

[30] Hermann Schlichting and Klaus Gersten. *Boundary-layer theory.* Springer, 2016.

[31] Hendrik Tennekes, John Leask Lumley, Jonh L Lumley, et al. *A first course in turbulence.* MIT press, 1972.

[32] David C Wilcox et al. *Turbulence modeling for CFD*, volume 2. DCW industries La Canada, CA, 1998.

[33] Joseph Smagorinsky. General circulation experiments with the primitive equations: I. The basic experiment. *Monthly Weather Review*, 91(3):99–164, 1963.

[34] W. W. Kim and S. Menon. An unsteady incompressible Navier-Stokes solver for large eddy simulation of turbulent flows. *I. J. for Numer. Meth. Fluids.*, 31:983–1017, 1999.

[35] Karin Klooster, Nick HT ten Hacken, Jorine E Hartman, Huib AM Kerstjens, Eva M van Rikxoort, and Dirk-Jan Slebos. Endobronchial valves for emphysema without interlobar collateral ventilation. *New England Journal of Medicine*, 373(24):2325–2335, 2015.

[36] A Paris. *Measuring velocity gradients in a particle-laden channel flow.* 1999.

[37] Tevfik Gemci, Timothy E Corcoran, and Norman Chigier. A numerical and experimental study of spray dynamics in a simple throat model. *Aerosol Science & Technology*, 36 (1):18–38, 2002.

[38] E Dekker. Transition between laminar and turbulent flow in human trachea. *Journal of applied physiology*, 16(6):1060–1064, 1961.

[39] Qunzhen Wang and Kyle D Squires. Large eddy simulation of particle-laden turbulent channel flow. *Physics of Fluids*, 8(5):1207–1223, 1996.

[40] P. Moin, K Squires, W Cabot, and Sangsan Lee. A dynamic subgrid-scale model for compressible turbulence and scalar transport. *Physics of Fluids A: Fluid Dynamics (1989-1993)*, 3(11):2746–2757, 1991.

[41] Franck Nicoud and Frédéric Ducros. Subgrid-scale stress modelling based on the square of the velocity gradient tensor. *Flow, turbulence and Combustion*, 62(3):183–200, 1999.

[42] Ugo Piomelli. Large-eddy simulation: achievements and challenges. *Progress in Aerospace Sciences*, 35(4):335–362, 1999.

[43] Ugo Piomelli and Elias Balaras. Wall-layer models for large-eddy simulations. *Annual review of fluid mechanics*, 34(1):349–374, 2002.

[44] Charles A Parker. Some observations and remarks on the air-currents in nasal respiration. *The Journal of Laryngology & Otology*, 16(7):345–355, 1901.

[45] Arthur W Proetz. Xli air currents in the upper respiratory tract and their clinical importance. *Annals of Otology, Rhinology & Laryngology*, 60(2):439–467, 1951.

[46] H Masing. Investigations about the course of flow in the nose model. *Arch. Klin. Exp. Ohr. Nas. Kehlkopf*, 189:371–381, 1967.

[47] Marc Girardin, Ertugrul Bilgen, and Pierre Arbour. Experimental study of velocity fields in a human nasal fossa by laser anemometry. *Annals of Otology, Rhinology & Laryngology*, 92(3):231–236, 1983.

[48] Christoph Brucker and Kyu-lk Park. Experimental study of velocity fields in a model of human nasal cavity by dpiv. 1999.

[49] SK Kim and SK Chung. An investigation on airflow in disordered nasal cavity and its corrected models by tomographic piv. *Measurement Science and Technology*, 15(6): 1090, 2004.

[50] Sung Kyun Kim and Seung-Kyu Chung. Investigation on the respiratory airflow in human airway by piv. *Journal of visualization*, 12(3):259–266, 2009.

[51] CG Ball, M Uddin, and A Pollard. Mean flow structures inside the human upper airway. *Flow, Turbulence and Combustion*, 81(1-2):155–188, 2008.

[52] A Johnstone. *Hot wire measurements in an oropharyngeal pathway.* PhD thesis, M. Sc. Thesis, Queen's University, Kingston, ON, Canada, 2002.

[53] WH Finlay, KW Stapleton, and J Yokota. On the use of computational fluid dynamics for simulating flow and particle deposition in the human respiratory tract. *Journal of Aerosol Medicine*, 9(3):329–341, 1996.

[54] Z Zhang, C Kleinstreuer, and CS Kim. Micro-particle transport and deposition in a human oral airway model. *Journal of Aerosol Science*, 33(12):1635–1652, 2002.

[55] Baoshun Ma and Kenneth R Lutchen. Cfd simulation of aerosol deposition in an anatomically based human large–medium airway model. *Annals of biomedical engineering*, 37 (2):271–285, 2009.

[56] A Putnam. Integratable form of droplet drag coefficient. *Ars Journal*, 31(10):1467–1468, 1961.

[57] DK LILLY. The representation of small-scale turbulence in numerical simulation experiments. In *Proc. IBM Sci. Compt. Symp. Environ. Sci., White Plains, IBM, 1967*, 1967.

[58] Massimo Germano, Ugo Piomelli, Parviz Moin, and William H Cabot. A dynamic subgrid-scale eddy viscosity model. *Physics of Fluids A*, 3(7):1760–1765, 1991.

[59] Ulrich Schumann. Subgrid scale model for finite difference simulations of turbulent flows in plane channels and annuli. *J. Comp. Phys.*, 18(4):376–404, 1975.

[60] S Menon and WW Kim. High Reynolds number flow simulations using the localized dynamic subgrid-scale model. *AIAA paper*, 425:1996, 1996.

[61] Shewen Liu, Charles Meneveau, and Joseph Katz. On the properties of similarity subgrid-scale models as deduced from measurements in a turbulent jet. *Journal of Fluid Mechanics*, 275:83–119, 1994.

[62] Cristian Marchioli. Large-eddy simulation of turbulent dispersed flows: a review of modelling approaches. *Acta Mechanica*, 228(3):741–771, 2017.

[63] Jacek Pozorski. Models of turbulent flows and particle dynamics. pages 97–150, 2017.

[64] Vincenzo Armenio, Ugo Piomelli, and Virgilio Fiorotto. Effect of the subgrid scales on particle motion. *Physics of Fluids*, 11(10):3030–3042, 1999.

[65] Henry G Weller, Gavin Tabor, Hrvoje Jasak, and Christer Fureby. A tensorial approach to computational continuum mechanics using object-oriented techniques. *Computers in physics*, 12(6):620–631, 1998.

[66] Raad I Issa. Solution of the implicitly discretised fluid flow equations by operator-splitting. *Journal of computational physics*, 62(1):40–65, 1986.

[67] Suhas V Patankar and D Brian Spalding. A calculation procedure for heat, mass and momentum transfer in three-dimensional parabolic flows. In *Numerical prediction of flow, heat transfer, turbulence and combustion*, pages 54–73. Elsevier, 1983.

[68] Graham B Macpherson, Niklas Nordin, and Henry G Weller. Particle tracking in unstructured, arbitrary polyhedral meshes for use in cfd and molecular dynamics. *Communications in Numerical Methods in Engineering*, 25(3):263–273, 2009.

[69] Andreas Schmidt, Stephan Zidowitz, Andres Kriete, Thorsten Denhard, Stefan Krass, and Heinz-Otto Peitgen. A digital reference model of the human bronchial tree. *Computerized Medical Imaging and Graphics*, 28(4):203–211, 2004.

[70] K-H Cheng, Y-S Cheng, H-C Yeh, and DL Swift. Measurements of airway dimensions and calculation of mass transfer characteristics of the human oral passage. 1997.

[71] Frantisek Lizal, Jakub Elcner, Philip K Hopke, Jan Jedelsky, and Miroslav Jicha. Development of a realistic human airway model. *Proceedings of the Institution of Mechanical Engineers, Part H: Journal of Engineering in Medicine*, 226(3):197–207, 2012.

[72] Frantisek Lizal, Miloslav Belka, Jan Adam, Jan Jedelsky, and Miroslav Jicha. A method for in vitro regional aerosol deposition measurement in a model of the human tracheobronchial tree by the positron emission tomography. *Proceedings of the Institution of Mechanical Engineers, Part H: Journal of Engineering in Medicine*, 229(10):750–757, 2015.

[73] Ching-Long Lin, Merryn H Tawhai, and Eric A Hoffman. Multiscale image-based modeling and simulation of gas flow and particle transport in the human lungs. *Wiley Interdisciplinary Reviews: Systems Biology and Medicine*, 5(5):643–655, 2013.

[74] Chantal Darquenne. Aerosol deposition in health and disease. *Journal of aerosol medicine and pulmonary drug delivery*, 25(3):140–147, 2012.

[75] Bruce G Miller. Fossil fuel emissions control technologies: Stationary heat and power systems. 2015.

[76] S. Song and J. K. Eaton. Flow structures of a separating, reattaching, and recovering boundary layer for a large range of Reynolds number. *Exp. in Fluids*, 36:642–653, 2004.

VITA

Divyajit Mahida was born in 1996 in Surat, India. He received his B. Tech. degree from School of Engineering and Applied Science, Ahmedabad University in 2018. In Fall 2019, he joined the College of Engineering and Computer Science at The University of Tennessee at Chattanooga to pursue graduate study in Mechanical Engineering-Energy. He had conducted research in the area of computational fluid dynamics under the guidance of Professor Reetesh Ranjan. His research interest includes the design, development, and application of high-performance numerical methods to perform fundamental investigation of turbulent flows. In May 2021 he would graduate with a Master of Science degree in Engineering from The University of Tennessee at Chattanooga.